Quantum phase transition in a two-dimensional Kondo-Heisenberg model: A dynamical Schwinger-boson large-*N* approach

Jiangfan Wang,[1] Yung-Yeh Chang,[1] Chung-Yu Mou,[2] Stefan Kirchner,[3,4] and Chung-Hou Chung[1,5]

[1]*Department of Electrophysics, National Chiao-Tung University, Hsinchu 30010, Taiwan, Republic of China*

[2]*Center for Quantum Technology and Department of Physics, National Tsing-Hua University, Hsinchu 30013, Taiwan, Republic of China*

[3]*Zhejiang Institute of Modern Physics and Department of Physics, Zhejiang University, Hangzhou 310027, China*

[4]*Zhejiang Province Key Laboratory of Quantum Technology and Device, Zhejiang University, Hangzhou 310027, China*

[5]*Physics Division, National Center for Theoretical Sciences, Hsinchu 30013, Taiwan, Republic of China*

(Received 14 August 2019; revised 14 August 2020; accepted 16 August 2020; published 15 September 2020)

We generalize the dynamical large-*N* multichannel Schwinger-boson approach to study the quantum phase transition of a two-dimensional Kondo-Heisenberg model, relevant for heavy electron systems, close to an antiferromagnetic Kondo destruction quantum critical point. By breaking up a Kondo singlet into a charge fermion (holon) and a bosonic spinon, we identify and characterize the quantum phase transition from an antiferromagnetically ordered state to a Kondo-dominated paramagnetic state, and attribute a jump in the holon phase shift to Kondo breakdown. We calculate transport and thermodynamic quantities. The global finite-temperature phase diagram and the critical behavior of various physical observables therein show a close resemblance to experimental observations.

DOI: 10.1103/PhysRevB.102.115133

I. INTRODUCTION

"Strange metal (SM)" behavior, which is characterized by a linear-in-temperature resistivity and a logarithmic-in-temperature specific-heat coefficient, has been reported in many strongly correlated electron systems close to onset of magnetization. The magnetic quantum critical points (QCP) are the result of competing order, and occur in a wide spectrum of quantum materials, including cuprate superconductors [1] and heavy electron systems [2]. The microscopic origin of this common phenomenology, however, has remained enigmatic.

Heavy electron materials often can be tuned from an antiferromagnetically ordered phase through a QCP to a paramagnetic Kondo-screened heavy Fermi liquid [3]. At the magnetic phase boundary, many heavy electron compounds and, in particular, $YbRh_2Si_2$ [4], $CeCu_{6-x}Au_x$ [5–8], and $CeMIn_5$ with M = Co, Rh [9,10], display SM behavior. Low-temperature measurements such as the spin susceptibility indicate that in the majority of these materials the effective low-energy degrees of freedom are two dimensional (2D), despite the three-dimensional (3D) crystal structure of theses materials [3,9,11,12]. Moreover, many experimental findings strongly suggest Kondo breakdown (KB) [13,14] to occur, a mechanism where the conventional quasiparticle description completely breaks down at the QCP, and the Kondo effect plays an important role in driving the phase transition. Among these experiments are Hall measurements [15] indicating a jump of the Fermi volume at $T = 0$, and neutron spectroscopy [7], optical conductivity [16], and STM measurements [17], pointing to ω/T scaling of various quantities at the transition.

These findings go beyond the standard Hertz-Millis type of spin-density-wave theory [18], critical quasiparticle approaches [19], and phenomenological approaches [20].

To account for the nature of the QCP, Doniach's framework for heavy electron systems where the Kondo effect competes with the nearest-neighbor antiferromagnetic (AF) interaction in the form of a Kondo-Heisenberg (KH) model is an appropriate starting point. Kondo breakdown in the KH model has been extensively studied by the extended dynamical mean-field theory (EDMFT) method [13,21,22], which covers the antiferromagnetically ordered and Kondo-screened heavy Fermi-liquid phases and captures the dynamical ω/T scaling in the quantum critical regime that reflects the dynamical competition between the Ruderman-Kittel-Kasuya-Yosida (RKKY) and Kondo interactions [23]. Several other techniques have also been used to study this problem [24–27], which capture aspects of the Kondo breakdown physics. An essential step to address the SM behavior is to study the global finite-temperature phase diagram as well as thermodynamics and transport properties near the Kondo breakdown QCP. In this paper, we take an alternative approach to this problem by using the dynamical large-*N* Schwinger-boson approach to the 2D KH model, generalized from the two-impurity Kondo model [28]. A simplified version of this approach on a one-dimensional (1D) Kondo lattice model to describe aspects of KB QCP was recently studied [29,30], where the AF ordered phase is absent, and the critical properties are expected to fall into a different universality class from that in two dimensional. However, it has not yet been applied to a two-dimensional lattice, allowing for long-range AF order to realistically capture the AF-KB transition seen experimentally. This method is able to describe both the antiferromagnetic phase through the condensation of bosons as well as aspects of the heavy electron phase.

Moreover, the breakup of a Kondo singlet into a charge fermion (holon) and a bosonic spinon has advantages in

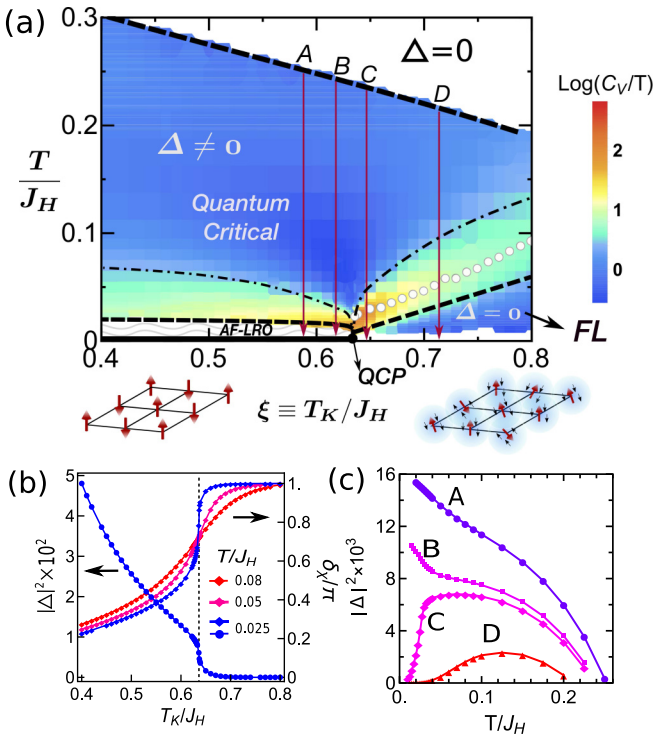

FIG. 1. (a) Phase diagram for $\kappa = 0.2$ mapped out using the specific-heat coefficient. The AF and heavy FL ground states are separated by a QCP at $\xi_c \approx 0.635$. Note that the AF-LRO phase only exists at $T = 0$ for the 2D KH model (bold solid line). The regions (light green) enclosed by the quantum critical region and the two stable ground states are the crossover regime. (b) $|\Delta|^2$ and the holon phase shift δ_χ/π as functions of ξ. (c) Temperature dependence of the magnetic short-range order $|\Delta|^2$ at different $\xi = T_K/J_H$ marked by A to D in (a).

addressing possible quasiparticle fractionalization at the KB QCP [25] and the emergent critical charge/spin fluctuations. We identify the antiferromagnetic Kondo breakdown (AF-KB) QCP [see Fig. 1(a)] via the holon phase shift linked to the Kondo hybridization and condensation of bosonic spinons. The global finite-temperature phase diagram and the critical behavior of various physical observables therein show a close resemblance to experimental observations.

II. HAMILTONIAN OF KONDO-HEISENBERG LATTICE MODEL

We start from the KH model on a square lattice,

$$H = H_0 + H_K + H_J, \tag{1}$$

where the Kondo term H_K and the AF interaction H_J are described as

$$H_K = J_K \sum_i \boldsymbol{S}_i \cdot \boldsymbol{\sigma}_i, \;\; H_J = J_H \sum_{\langle i,j\rangle} \boldsymbol{S}_i \cdot \boldsymbol{S}_j, \tag{2}$$

respectively. In Eq. (2), the Kondo coupling J_K and the AF interaction J_H are treated to be independent of each other for generality. Here, $H_0 = \sum_{\boldsymbol{p}a\alpha} \varepsilon_{\boldsymbol{p}} \psi^\dagger_{\boldsymbol{p}a\alpha} \psi_{\boldsymbol{p}a\alpha}$ describes the noninteracting conduction electron part of the model with $\psi^\dagger_{\boldsymbol{p}a\alpha}$ being the creation operator of a conduction electron with quasimomentum $\boldsymbol{p}$ with channel index $a \in [1, K]$ and spin index $\alpha \in \{-\frac{N-1}{2}, -\frac{N-1}{2}+1, \ldots, \frac{N-1}{2}-1, \frac{N-1}{2}\}$. The large-$N$ [Sp(N)] generalization of H in the Schwinger-boson representations reads as [28]

$$\begin{aligned} H \to H_0 &+ \sum_{i,a,\alpha} \left[\frac{1}{\sqrt{N}} (b^\dagger_{i\alpha} \psi_{ia\alpha}) \chi_{ia} + \text{H.c.} + \frac{|\chi_{ia}|^2}{J_K} \right] \\ &+ \sum_{\langle i,j\rangle,\alpha} \left[\text{sgn}(\alpha) b_{i\alpha} b_{j,-\alpha} \Delta_{\text{ij}} + \text{H.c.} + \frac{N|\Delta_{\text{ij}}|^2}{J_H} \right] \\ &+ \sum_i \lambda_i [n_b(i) - 2S]. \end{aligned} \tag{3}$$

In Eq. (3), $\psi^\dagger_{ia\alpha}$ is the Fourier component of $\psi^\dagger_{\boldsymbol{p}a\alpha}$ with i being the site index. The Schwinger-boson operator $b^\dagger_{i\alpha}$ creates a spinon of spin α. Note that the large-N generalization to the local spin operator $\boldsymbol{S}_i$ at site i can be expressed in terms of either the N-flavored bilinear fermions [31] or bosons [28–30,32]. The Kondo hybridization in this formulation, $\chi_{ia} \propto \sum_\alpha \langle \psi^\dagger_{ia\alpha} b_{i\alpha} \rangle$, is a charged, spinless fermionic holon field obtained through decoupling of the original Kondo term. Unlike the pseudofermion representation of spins, here χ does not break a gauge symmetry, i.e., $\langle \chi_{ia} \rangle \equiv 0$. On the paramagnetic side electrons and spinons form bound Kondo singlets. An energy gap appears in both the spinon and holon spectrum which protects the spin singlets from being destroyed by thermally excited spinons [33]. As a result, various physical quantities exhibit Fermi-liquid behavior at low temperatures. On the other hand, the absence of the Kondo resonance peak at the Fermi energy due to the holon gap is an artifact of our approach [see Appendix C].

The AF Heisenberg interaction H_J is expressed in terms of the Sp(N)-invariant resonating valence bond (RVB) term, $\text{sgn}(\alpha) b_{i\alpha} b_{j,-\alpha} \Delta_{\text{ij}}$, where $\Delta_{\text{ij}} = -\frac{N}{J_H} \sum_\alpha \langle \text{sgn}(\alpha) b^\dagger_{j,-\alpha} b^\dagger_{i\alpha} \rangle$ is the AF short-range order (SRO) parameter. A SRO bosonic spin liquid may appear in systems with strong magnetic frustration and/or disorder. The AF long-range order (LRO) phase is represented in terms of gapless spinon excitations or equivalently a nonvanishing boson condensate $\langle b_{i\alpha} \rangle \neq 0$ [34]. The capability of describing both LRO and SRO is a major advantage of our approach over the fermionic representation. The last term in H enforces the constraint $n_b(i) = \sum_\alpha \langle b^\dagger_{i\alpha} b_{i\alpha} \rangle = 2S$, where $2S = K$ corresponds to exact spin screening [28]. We will assume that $\lambda_i = \lambda$, and $\Delta_{i,i+\hat{x}} = \Delta_{i,i+\hat{y}} = \Delta$. The ratio $\kappa \equiv K/N$ is kept constant ($\kappa = 0.2$ here [35]) as we take the large-N limit.

III. METHOD

To solve Eq. (3), we exploit the self-consistent Dyson-Schwinger equations in terms of the fully dressed Green's functions and self-energies. We assume that all the self-energies are momentum independent, i.e., $\Sigma(i\omega, \boldsymbol{p}) \to \Sigma(i\omega)$, similar to what is used in the DMFT. Due to the local nature at the KB QCP [13], we expect this local approximation captures various aspects of the transition though the long-ranged fluctuations are neglected. The resulting local Green's

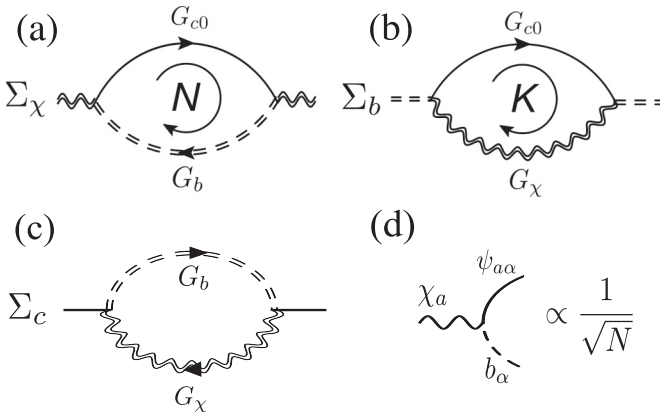

FIG. 2. The Feynman diagrams for the self-energy of (a) the holon field χ, Σ_χ, (b) the Schwinger boson b, Σ_b, and (c) the conduction electron, Σ_c. (d) The bare vertex of the Kondo term contributes a factor of $1/\sqrt{N}$. The double dashed (wavy) line denotes the *full* Green's function of the Schwinger-boson b (χ) field. The single solid line represents the *bare* Green's function of the conduction electrons.

functions read as

$$G_{c0}(i\omega) = \sum_{\boldsymbol{p}} \frac{1}{i\omega - \varepsilon_{\boldsymbol{p}}},\ G_b(i\nu) = \sum_{\boldsymbol{p}} \frac{-\gamma_b(-i\nu)}{4|\Delta|^2\xi_{\boldsymbol{p}}^2 - \Gamma(\nu)},$$
$$G_\chi(i\omega) = [-J_K^{-1} - \Sigma_\chi(i\omega)]^{-1}, \tag{4}$$

and

$$\Sigma_\chi(i\omega) = \frac{1}{\beta}\sum_\nu G_{c0}(i\nu - i\omega)G_b(i\nu),$$
$$\Sigma_b(i\nu) = -\frac{\kappa}{\beta}\sum_\omega G_{c0}(i\omega + i\nu)G_\chi(-i\omega). \tag{5}$$

In the above equations, $\omega \equiv \pi(2n+1)/\beta$ and $\nu \equiv 2\pi n/\beta$ denote the fermionic and bosonic Matsubara frequencies, and $\varepsilon_{\boldsymbol{p}}$ the conduction electron dispersion. In Eq. (4), $\Gamma(\nu) \equiv \gamma_b(i\nu)\gamma_b(-i\nu)$ and $\gamma_b(z) \equiv z - \lambda - \Sigma_b(z)$, and $\xi_{\boldsymbol{p}} = \sin p_x + \sin p_y$ is the bare dispersion of the spinon on a square lattice. We keep the leading terms in Σ_b and Σ_χ of order of unity (Fig. 2), but ignore the vertex corrections and the conduction electron self-energy Σ_c, which are of higher order in $1/N$, i.e., $\Sigma_c(i\omega) = (1/N\beta)\sum_\nu G_b(i\nu - i\omega)G_\chi(i\nu)$.

Two constraints for the Green's functions are obtained by minimizing the free energy with respect to λ and Δ:

$$\kappa = \frac{-1}{\beta}\sum_\nu G_b(i\nu),\ \frac{1}{J_H} = \frac{-1}{\beta}\sum_{\boldsymbol{p},\nu}\frac{\xi_{\boldsymbol{p}}^2}{4|\Delta|^2\xi_{\boldsymbol{p}}^2 - \Gamma(\nu)}. \tag{6}$$

The unknowns, $G_\chi(\omega)$, $G_b(\nu)$, $\Sigma_\chi(\omega)$, $\Sigma_b(\nu)$, λ, and Δ, are obtained self-consistently through Eqs. (4)–(6). Note that Eqs. (4)–(6) go beyond the static large-N mean-field saddle-point solutions, and are capable of describing non-Fermi-liquid (NFL) behaviors [28–30,33].

IV. RESULTS

A. Global phase diagram

Our main results are summarized in Fig. 1(a): a phase diagram in terms of the tuning parameter $\xi \equiv T_K/J_H$ ($T_K = De^{-D/J_K}$ is the bare Kondo temperature with D being the half-bandwidth of the conduction electrons) and the temperature T/J_H is mapped out via the specific-heat coefficient C_V/T. Here, we set $\kappa = 0.2$, at the brink of AF-LRO ground state in the 2D Heisenberg limit: the AF-LRO phase exists for $\kappa \geqslant 0.2$ [32,36]. At $T = 0$, a QCP at $\xi = \xi_c$, separating AF-LRO phase at small ξ and the paramagnetic FL ground state at large ξ is clearly identified via the low-temperature evolution of various quantities. The AF-LRO phase can be inferred from the gapless spinon excitations (or equivalently the development of boson condensation $\langle b\rangle \neq 0$), while the heavy Fermi liquid (FL) phase is identified through the linear-in-T entropy and the holon phase shift δ_χ, defined as

$$\frac{\delta_\chi}{\pi} = -\mathrm{Im}\ln[1 + J_K\Sigma_\chi(i0^+)]. \tag{7}$$

Within the FL phase, the magnetic SRO vanishes, and both the spinons and holons develop gaps in their spectral functions. The abrupt jump of the holon phase shift δ_χ/π [Fig. 1(b)], and for $\xi > \xi_c$, the vanishing of $|\Delta|^2$ as $T \to 0$ [Fig. 1(c)] indicate a reconstruction of the Fermi surface at the QCP [see Appendix C], which is consistent with the Kondo breakdown observed in various heavy electron compounds including $YbRh_2Si_2$ [15] and $CeCu_{6-x}Au_x$ [7,8]. For illustration, we consider a finite N and calculate the conduction electron spectral density $(-1/\pi)\mathrm{Im}G_c(\boldsymbol{p},\omega)$ with $G_c^{-1}(\boldsymbol{p},\omega) = \omega - \varepsilon_{\boldsymbol{p}} - \Sigma_c(\omega)$ by including the conduction electron self-energy Σ_c self-consistently [Fig. 2(c)], and find that a Kondo hybridization gap opens near the Fermi energy [Fig. 3(a) and Appendix C]. In addition, $|\Delta| \to 0$ indicates the complete suppression of the AF-SRO in the heavy FL phase [28–30]. We find an AF-LRO ground-state phase to persist at finite temperature [Fig. 1(a)]. However, the finite-temperature AF-LRO phase is ruled out by the Mermin-Wagner theorem [37] and thus is an artifact of our approach (see the Discussions and Appendix C). The holon and spinon gaps both close at the QCP and in the AF phase, giving rise to singular-in-T observables.

B. Entropy and specific-heat coefficient

Figure 4 shows the temperature dependence of the entropy S [38] where

$$\frac{S}{N} = \frac{\beta^2}{\pi}\int d\nu\left[\frac{dn_B}{d\beta}\left(\frac{1}{2\mathcal{N}_s}\sum_{\boldsymbol{p}}\mathrm{Im}\ln\det\left[-\mathbf{G}_b^{-1}(\boldsymbol{p},\nu)\right] + \Sigma_b''G_b'\right) + \kappa\left[\frac{dn_F}{d\beta}\left(\mathrm{Im}\ln\left[-G_\chi^{-1}\right] + \Sigma_\chi''G_\chi' - N\Sigma_c'G_{c0}''\right)\right]\right] \tag{8}$$

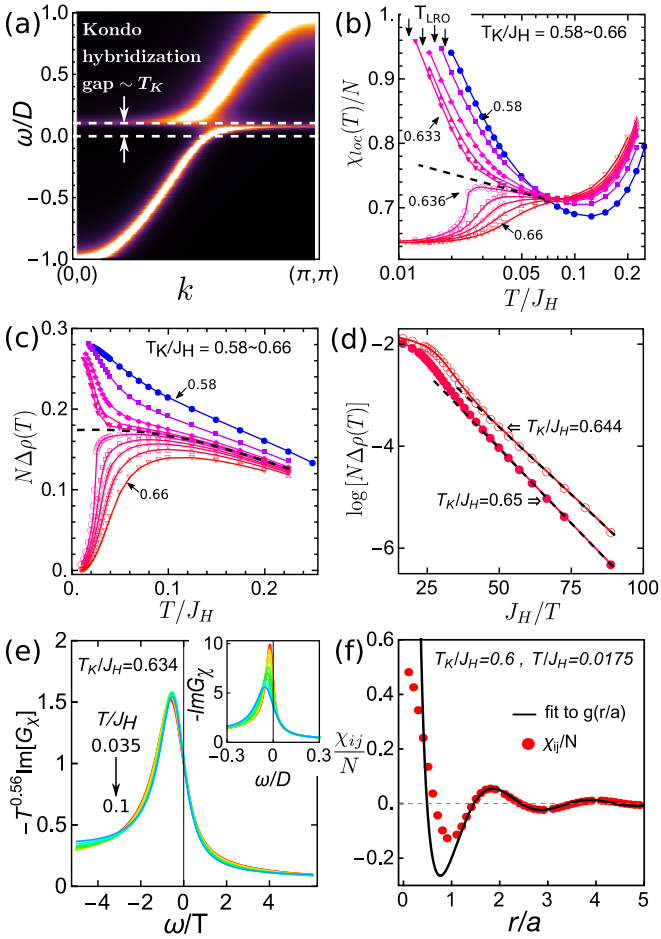

FIG. 3. (a) The conduction-electron spectral function $(-1/\pi)\mathrm{Im}G_c(\boldsymbol{k},\omega)$ in terms of momentum k and frequency ω for $N = 10$, $K = 2$ with $T_K/D = 0.082$, $\xi = 0.874$, and $T/T_K = 0.12$. The hybridization gap is of order of T_K. (b) Temperature dependence of the local spin susceptibility $\chi_{\mathrm{loc}}(T)/N$ at different values of ξ. Arrows indicate the onset temperature of AF LRO, T_{LRO}. (c) Temperature-dependent electrical resistivity $\rho(T)$ with different values of ξ. The dashed lines in (b) and (c) schematically show the extrapolations of $\chi_{\mathrm{loc}}(T)$ and $\rho(T)$ at the QCP. (d) The resistivity behaves as $\rho(T) \sim \exp(-J_H/T)$, fitted by the dashed lines, in the lower-temperature regime. (e) The imaginary part of G_χ exhibits ω/T behavior near the QCP ($\xi = 0.634$). Inset: G''_χ without being scaled. (f) Spatial dependence of the spin susceptibility along the x direction, χ_{ij}/N (red dots), fitted to $g(r/a) \equiv (a^2/5r^2)\cos(3.21r/a)$ (solid curve) with $\vec{r}_i - \vec{r}_j \equiv (r, 0)$ and a being the lattice constant.

with

$$-\mathbf{G}_b^{-1}(\boldsymbol{p},\nu) = \begin{pmatrix} -\gamma_b(\nu) & 2i\Delta\xi_{\boldsymbol{p}} \\ -2i\Delta^*\xi_{\boldsymbol{p}} & -\gamma_b(-\nu) \end{pmatrix}, \tag{9}$$

and the specific-heat coefficient $\gamma \equiv C_V/T = \partial S/\partial T$ at different values of ξ. For $\xi > \xi_c$, and at low temperatures, the specific-heat coefficient develops a plateau, reflecting the formation of a FL state with $S \sim T$ (see inset of Fig. 4). As ξ approaches ξ_c from the Kondo side, the temperature range of the plateau shrinks monotonically and vanishes at the QCP. Above the FL region, the specific-heat coefficient increases until it reaches a "Schottky" peak (see Fig. 4).

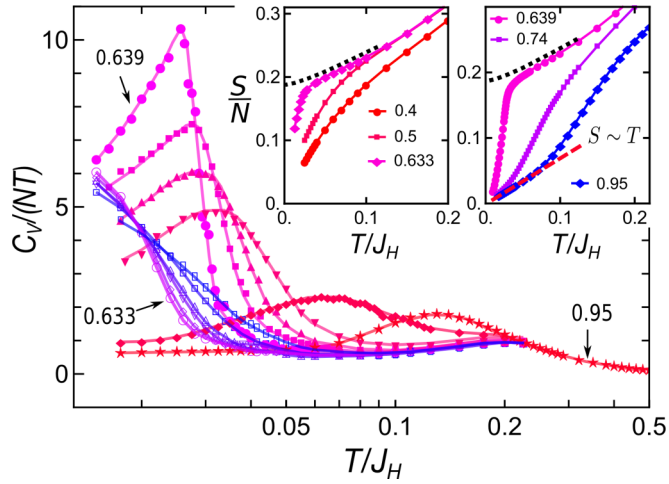

FIG. 4. Temperature dependence of C_V/NT at different values of ξ [from $\xi = 0.61$ (blue) to $\xi = 0.95$ (red)]. Inset: entropy per spin as functions of temperature at $\xi < \xi_c$ (left) and $\xi > \xi_c$ (right), respectively. At $T = 0$, there is a residual entropy at the QCP, as indicated by the black dotted curves.

Note that the peak temperatures [open circles in Fig. 1(a)] display a weakly first-order jump at the QCP [29,39,40]. The collapse of energy scales from both sides as the QCP is approached is clearly seen in the color map of the γ coefficient [Fig. 1(a)] with a fan-shaped quantum critical region. A large residual ($T = 0$) entropy $S/N \sim 0.2$ is found at the QCP.

Including finite-N fluctuations, we found this residual entropy still survives, as indicated in Appendix G. We suspect that the residual entropy is due to the local character of our approximation, which will be addressed elsewhere.

C. Magnetic susceptibility

The static local (momentum-integrated) magnetic susceptibility $\chi_{\mathrm{loc}}(T)$ as a function of temperature for $T > T_{\mathrm{LRO}}$ defined as

$$\frac{\chi_{\mathrm{loc}}(T)}{N} = 2\int \frac{dz}{\pi} n_B(z) G_b'(z) G_b''(z) \tag{10}$$

is plotted in Fig. 3(b) at different values of ξ near the QCP. Note that we consider the direction of the applied field is parallel to the orientation of sublattice magnetization (see Appendix E). Besides, in this work we only self-consistently calculate $\chi_{\mathrm{loc}}(T)$ in the temperature range of $T \geqslant T_{\mathrm{LRO}}$ for $\xi < \xi_c$. The local magnetic susceptibility $\chi_{\mathrm{loc}}(T)$ shows two distinct properties corresponding to the two regimes $\xi > \xi_c$ and $\xi < \xi_c$ as $T/J_H \to 0$. In the Kondo limit, the susceptibility displays a crossover from a saturated Pauli susceptibility at low temperatures, where all the local spins are fully screened, to a typical spin-liquid behavior at relatively high temperatures [41]. As expected, at temperatures well above the spin-liquid region, the local susceptibility exhibit a $1/T$ behavior [see Appendix E]. Furthermore, χ_{loc} shows a power-law divergence at low T on the AF side due to the softened spinon gap in proximity to LRO. The quantum critical fan is identified in our calculations through the power-law scaling of the local susceptibility, as illustrated in Appendix E.

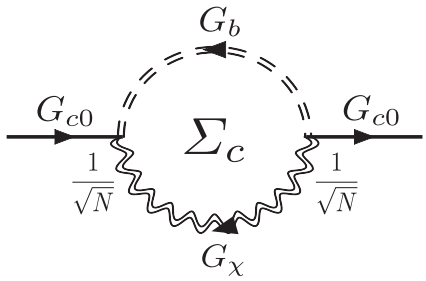

FIG. 5. The one-loop diagram of $\Sigma_c(\omega)$.

To obtain the susceptibility for $T < T_{\rm LRO}$, one needs to include the condensed Schwinger bosons, $x_{i\alpha} \equiv \langle b_{iv\alpha}\rangle = \langle b^\dagger_{iv\alpha}\rangle$, into our self-consistent equations (only one particular spin flavor gets condensed at each particular site), which is technically challenging and is not the main focus of this work. Although we did not self-consistently calculate the spin susceptibility for $T < T_{\rm LRO}$, we qualitatively estimate the low-temperature behavior of susceptibility for temperatures $T \leqslant T_{\rm LRO}$, where the condensate of Schwinger boson $x_{i\alpha}$ is developed: $b_{iv\alpha} = x_{i\alpha} + \delta b_{iv\alpha}$ with $\delta b_{iv\alpha}$ being the fluctuating boson field. The condensate $x_{i\alpha}(T)$ increases with decreasing T until all bosons are condensed and $\langle \delta b^\dagger_{iv\alpha}\delta b_{iv\alpha}\rangle = 0$ at $T = 0$. As is shown in Appendix E, by the fluctuation-dissipation theorem, spin susceptibility depends only on the correlations of the fluctuating boson fields $\langle \delta b \delta b^\dagger\rangle$, and does not explicitly depend on the condensate fields $x_{i\alpha}$ [see Eq. (E10)]. As a result, for $T < T_{\rm LRO}$, the local spin susceptibility $\chi_{\rm loc}(T)$ monotonically decreases as the boson fluctuation is gradually suppressed by the enhanced boson condensation with the decreasing of temperature, and eventually reach its minima as $T \to 0$ where the boson condensation completely develops. A simple calculation for spin susceptibility $\chi_{\rm ij}$ between sites i and j at $T = 0$ can confirm the above qualitative estimation: Since all bosons are condensed at $T = 0$, the spin susceptibility $\chi_{\rm ij}$ of Eq. (E3) reads as

$$\chi_{\rm ij} = \langle M_i M_j\rangle - \langle M_i\rangle\langle M_j\rangle = \sum_{vv'\alpha\alpha'} {\rm sgn}(\alpha){\rm sgn}(\alpha')\left[x^2_{i\alpha}x^2_{j\alpha'} - x^2_{i\alpha}x^2_{j\alpha'}\right] \to 0, \qquad (11)$$

where the z-direction sublattice magnetization of local spin can be estimated as $M_i = \sum_{v\alpha} {\rm sgn}(\alpha) b^\dagger_{iv\alpha} b_{iv\alpha} = \sum_{v\alpha} {\rm sgn}(\alpha) x^2_{i\alpha}$ for $T = 0$. Combining the above estimations and calculations, we expect that $\chi_{\rm loc}$ starts to decrease as the system enters the LRO phase, and eventually vanish as $T \to 0$. The above argument and calculations also apply to the uniform spin susceptibility $\chi_{\rm uni}$ (see Appendix E).

D. Electrical resistivity

Figure 3(c) shows the electrical resistivity obtained through the Boltzmann formula [42]

$$\rho^{-1}(T) = -\frac{ne^2}{m}\int \tau(\omega)\frac{\partial n_F(\omega)}{\partial\omega}d\omega, \qquad (12)$$

where $n_F(x) \equiv [\exp(x/T)+1]^{-1}$ denotes the Fermi function and $\tau^{-1}(\omega) = -2\Sigma''_c(\omega) \propto O(1/N)$ is the scattering rate of the conduction electrons (see Fig. 5). At low and with decreasing temperatures, electrical resistivity shows a singular increase on the AF side due to softened spinon gap close to LRO, while it decreases on the heavy FL side as a result of developing coherent Kondo hybridization (holon) gap. The qualitative features are consistent with that seen in $CeCu_{6-x}Au_x$ and are somewhat reminiscent of a metal-to-insulator transition [6], where apart from the AF-KB QCP, the short-ranged AF spin fluctuations have also been seen experimentally [3].

Note that, to leading order in N, the expected T^2 Fermi-liquid behavior is replaced by an exponential decay [Fig. 3(d)], due to the finite holon and spinon gaps [33]. To recover the T^2 resistivity, one needs to include the contributions to the scattering rate of order $O(1/N^2)$ [33].

E. ω/T scaling

The ω/T scaling has initially been observed in the dynamical spin response [7], and connected to the critical Kondo breakdown [22,26,30]. More recently, dynamical scaling has also been demonstrated in the charge response [43] and observed in optical conductivity measurements on $YbRh_2Si_2$ [16], which is thus believed to be induced by the emergent critical charge fluctuations at the KB QCP. This observation is further supported by the ω/T scaling of the critical valence fluctuations in G_χ at the KB QCP, i.e., $G''_\chi(\omega, T) = -T^{0.56} f(\omega/T)$ with $f(\omega/T)$ being a universal function [see Fig. 3(e)]. The weakly first-order transition at the QCP ξ_c, similar to the jump of the position of Schottky peak of specific-heat coefficient near the QCP (see Fig. 1), also reflects on the slight shift of peak position of the holon spectrum $-G''_\chi(\omega)$ as one goes from one side of the QCP to the other [see Appendix C]. We also observed that $G''_\chi(\omega)$ does not peak at $\omega = 0$, violated with the result in Ref. [30]. We suspect that it is likely due to the particle-hole asymmetry of our model.

V. EFFECT OF $1/N$ FLUCTUATIONS

To examine the stability of the infinite-N results against the finite-N fluctuations, we include the contributions of the full Green's function G_c and the self-energy Σ_c of the conduction electrons in our self-consistent Schwinger-Dyson equations in Eq. (2) (we set $N = 10$ here).

Before we present our finite-N results, we would like to make a remark concerning our finite-N approach: To fully address the finite-N corrections, in general, we also need to include fluctuations of the Lagrange multiplier λ and the corrections higher than $O(1/N)$. However, the restriction to the $1/N$ correction in only Σ_c which we used here may still be reliable to some extent, at least in the finite-N SU(N) Schwinger-boson method to the infinite-U Anderson model, as studied in Ref. [33]. This approach is capable of reproducing the Langreth sum rule (Friedel sum rule for Anderson's model) in the Fermi liquid [33], which cannot be addressed in the strict large-N limit. This suggests that the fluctuations of λ and other corrections higher than $1/N$ are not likely to play a significant role here. Nonetheless, a proper analysis of the $1/N$ corrections although technically challenging may shed light on the overall stability of the fixed point.

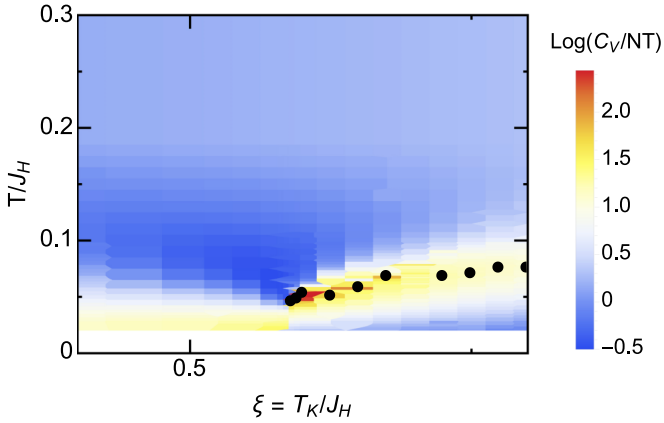

FIG. 6. The finite-temperature phase diagram with the inclusion of finite-N correction: a QCP can be seen at $T_K/J_H \sim 0.517$. The dark circle marks the position of the Schottky peak which indicates the onset of Fermi-liquid phase.

The self-consistent equations for G_c and Σ_c can be obtained as

$$G_c^{-1}(\omega) = G_{c0}^{-1}(\omega) - \Sigma_c(\omega),$$
$$\Sigma_c(\omega) = \frac{1}{N\beta}\sum_{\nu} G_b(\nu-\omega)G_\chi(\nu) \propto O(1/N). \quad (13)$$

In addition to the inclusion of self-consistent equations of G_c and Σ_c, we also have to replace G_{c0} by G_c which appears in the self-consistent equations of the infinite-N case [Eqs. (4) to (6)]. It turns out that the finite-temperature phase diagram (Fig. 6), the ω/T scaling, as well as various thermodynamic observables are in close resemblance to the large-N results except for some quantitative changes. Details are provided in Appendix G. We thus believe that the large-N approach is robust against the $1/N$ fluctuations arising from the conduction electron self-energy, and the large-N results are able to correctly describe the qualitative features of the finite-temperature phase diagram.

VI. DISCUSSIONS

The origin of the AF-LRO phase at finite temperatures we found for $J_K \neq 0$ and $J_H \neq 0$, which violates the Mermin-Wagner theorem, deserves further discussions. In the 2D Heisenberg limit ($J_K = 0$, $J_H \neq 0$), we did not obtain the finite-temperature AF-LRO phase. The evolution of the spinon gap $\lambda - 4|\Delta|$ with temperature at the low-temperature regime follows the trend of $(a/T)\exp(-b/T)$ with a, $b > 0$ being constants and thus is nonvanishing at finite temperatures (see Appendix C). This is in agreement with Mermin-Wagner theorem and the results of the large-N [SU(N)] Schwinger-boson approach to the 2D antiferromagnetic Heisenberg model by Arovas and Auerbach [32,36]. In contrast to the 2D Heisenberg limit, for the more general case where $J_K \neq 0$ and $J_H \neq 0$, we found that the spinon gap $|\lambda + \mathrm{Re}\Sigma_b(i0^+)| - 4|\Delta|$ with Σ_b being the Schwinger-boson self-energy, vanishes at a particular $T \neq 0$ [see Appendix C], suggesting the onset of finite-temperature AF-LRO state. We therefore conclude that it is Σ_b that leads to the formation of AF LRO and the associated long-range behavior in the position-dependent spin-spin correlations χ_{ij} [see Fig. 3(f)] in the presence of finite Kondo coupling [44]. It is expected that a proper treatment of nonlocal correlations beyond the local approximation will remedy this problem [45]. Likewise, the violation of Mermin-Wagner theorem in our finite-temperature AF-LRO phase when $J_K \neq 0$, $J_H \neq 0$ is likely due to the neglect of momentum dependence in the self-energies. We think that neglecting the momentum-dependent self-energies may simultaneously make us neglect the effect of long-wavelength spin fluctuations of the RKKY interaction induced by Kondo coupling, which, via the Mermin-Wagner theorem, is responsible for destroying the magnetic order in low-dimensional systems. This will lead to the formation of AF-LRO state at finite temperatures as we show in our finite-temperature phase diagram.

At nonzero temperatures, the region with $|\Delta| \neq 0$ extends to the quantum critical region. We attribute this feature to the bosonic representation of impurity spins where the holon field χ retains its $\langle\chi\rangle = 0$, giving rise to an overestimated RVB mean field Δ. Introducing a combined boson-fermion supersymmetric representation of spins [46] may remedy this artifact. We checked that the qualitative features of our large-N results are robust against finite-N fluctuations, as shown in Appendix G. Meanwhile, whether the residual entropy at the QCP can survive beyond the local approximation needs further investigations [30,47,48]. Near the LRO phase boundary, topological excitations related to the Berezinskii-Kosterlitz-Thouless (BKT) physics, which may affect the critical properties, have not been considered here [49], and will be addressed elsewhere [50]. There are other approaches to this model: A fermionic mean-field analysis of the K-H model on square lattice shows the similar competition between Kondo and AF ground states. Nevertheless, the critical properties are out of reach within this approach [51]. A renormalization group (RG) analysis of this model on the square lattice shows the breakdown of hydrodynamic behavior as the spin-wave velocity is suppressed logarithmically [52].

VII. CONCLUSIONS

We have generalized the dynamical large-N [Sp(N)] multichannel Schwinger-boson approach to explore the quantum phase transition and the quantum criticality of heavy electron compounds in an antiferromagnetic Kondo-Heisenberg model on a two-dimensional lattice reflecting the realistic quasi-2D nature of the materials. Our approach efficiently captures important aspects of the antiferromagnetic Kondo breakdown quantum critical point, separating the antiferromagnetic long-range order phase from the Kondo-screened heavy Fermi-liquid phase. The finite-temperature phase diagram is similar to that of $YbRh_2Si_2$ and $CeCu_{6-x}Au_x$.

The calculated resistivity profile near criticality and the ω/T scaling in the emergent critical charge fluctuations show a close resemblance to $CeCu_{6-x}Au_x$ and $YbRh_2Si_2$, respectively. Further theoretical and experimental studies to clarify the strange metal behaviors are needed.

ACKNOWLEDGMENTS

The authors acknowledge discussions with P. Coleman, Y. Komijani, G. Kotliar, S. Paschen, and Q. Si. This work is supported by the MOST (Grant No. 107-2112-M-009-010-MY3), the NCTS of Taiwan, Republic of China (C.-H.C.); Center for Quantum Technology funded by MOE of Taiwan (C.-Y. M.); the National Key R&D Program of the MOST of China, Grant No. 2016YFA0300202 and the National Science Foundation of China, Grant No. 11774307 (S.K.). S.K. acknowledges support by MOST of Taiwan, Grant No. 108-2811-M-009-500, and the hospitality of NCTU, Hsinchu, Taiwan.

APPENDIX A: DERIVATION OF THE SELF-CONSISTENT EQUATIONS

In this Appendix, we provide detailed derivations for the self-consistent Schwinger-Dyson equations for the large-N [Sp(N)] approach to the Kondo-Heisenberg model.

The path-integral action for the Kondo-Heisenberg model of Eq. (3) can be written as

$$\begin{aligned} S = &- \sum_{\boldsymbol{p}\omega a\alpha} \psi^*_{\boldsymbol{p}\omega a\alpha}(i\omega - \varepsilon_{\boldsymbol{p}})\psi_{\boldsymbol{p}\omega a\alpha} - \sum_{\boldsymbol{p}\nu\alpha} b^*_{\boldsymbol{p}\nu\alpha}(i\nu - \lambda)b_{\boldsymbol{p}\nu\alpha} \\ &+ \frac{1}{\sqrt{N}} \sum_{\boldsymbol{p}k\omega\nu a\alpha} b^*_{\boldsymbol{p}\nu\alpha}\psi_{\boldsymbol{k}\omega a\alpha}\chi_{\boldsymbol{p}-k,\nu-\omega,a} + \text{H.c.} \\ &- i\bar{\Delta}\sum_{\boldsymbol{p}\nu\alpha} \text{sgn}(\alpha) b_{\boldsymbol{p}\nu\alpha}b_{-\boldsymbol{p},-\nu,-\alpha}\xi_{\boldsymbol{p}} + \text{H.c.} + S_0 \\ &+ \sum_{\boldsymbol{p}\omega a} \frac{|\chi_{\boldsymbol{p}\omega a}|^2}{J_K} + S_0. \end{aligned} \tag{A1}$$

Here, $S_0 = \beta N \mathcal{N}_s(2|\Delta|^2/J_H - \lambda\kappa)$ is a constant. For simplicity, the measure $1/(\beta\mathcal{N}_s)$ associated with each sum of momentum and frequency has been dropped.

Note that, in Eq. (A1), the fields $\psi_{\boldsymbol{p}\omega a\alpha}$ and $b_{\boldsymbol{p}\nu\alpha}$ carry a dimension of the inverse of energy, while the holon field $\chi_{\boldsymbol{p}\omega a}$ is dimensionless. The parameters β^{-1}, λ, Δ, J_H, and J_K all have the dimension of energy. Within our calculations, we take the half-bandwidth of conduction electron D as the energy unit, i.e., taking $\beta \to \beta D^{-1}$, $\lambda \to \lambda D^{-1}, \ldots$ in Eq. (A1) so that all of them are dimensionless.

The equations of motion (EOM) for the dynamic fields (b, ψ, χ) can be derived using the standard generating function

$$Z[I, J, K] = \int_{b,\psi,\chi} e^{-S} \exp[I^\dagger b + J^\dagger\psi + K^\dagger\chi + \text{H.c.}], \tag{A2}$$

where I, J, and K are the external sources coupled to the three fields b, ψ, and χ (I is an ordinary complex field, while J and K are Grassmann fields), with $I^\dagger b \equiv \sum_{\boldsymbol{p}\nu\alpha} I^*_{\boldsymbol{p}\nu\alpha}b_{\boldsymbol{p}\nu\alpha}$ and so on. Note that the external sources I, J, and K will be set to zero at the end of derivation.

The EOM can be obtained via the fact that the functional integral of Eq. (A2) is invariant under infinitesimal variation of the integral variables b, ψ, and χ. First of all, the EOM corresponding to the variation of the b field, $b \to b + \delta b$, are given by

$$\begin{aligned} 0 = \frac{1}{Z}\frac{\delta Z}{\delta b^*_{p\nu\alpha}} &= (i\nu - \lambda)\langle b_{p\nu\alpha}\rangle - 2i\Delta\,\text{sgn}(\alpha)\xi_p\langle b^*_{-p,-\nu,-\alpha}\rangle \\ &- \frac{1}{\sqrt{N}}\sum_{k\omega a}\langle\psi_{k\omega a\alpha}\chi_{p-k,\nu-\omega,a}\rangle + I_{p\nu\alpha} \end{aligned} \tag{A3}$$

and

$$\begin{aligned} \frac{1}{Z}\frac{\delta Z}{\delta b_{-p-\nu-\alpha}} &= -(i\nu + \lambda)\langle b^*_{-p-\nu-\alpha}\rangle + 2i\bar{\Delta}\,\text{sgn}(\alpha)\xi_p\langle b_{p\nu\alpha}\rangle \\ &- \frac{1}{\sqrt{N}}\sum_{k\omega a}\langle\chi^*_{-p-k,-\nu-\omega,a}\psi^*_{k\omega a,-\alpha}\rangle + I^*_{-p-\nu-\alpha} \\ &= 0, \end{aligned} \tag{A4}$$

where $\langle O\rangle \equiv \frac{1}{Z}\int_{b,\psi,\chi} Oe^{-S+I^\dagger b+J^\dagger\psi+K^\dagger\chi+\text{H.c.}}$ denotes the statistical average of O in the presence of external sources. There are another four EOMs corresponding to the transformations of the ψ and χ fields, $\psi \to \psi + \delta\psi$ and $\chi \to \chi + \delta\chi$.

The Dyson-Schwinger equations for the Green's function of the spinon field b can be derived through the functional derivative of the EOM of Eqs. (A3) and (A4) with respect to $I_{p\nu\alpha}$, yielding

$$\begin{aligned} &-(i\nu - \lambda)\langle b_{p\nu\alpha}b^*_{p\nu\alpha}\rangle_c + 2\,\text{sgn}(\alpha)i\Delta\xi_p\langle b^*_{-p,-\nu,-\alpha}b^*_{p\nu\alpha}\rangle_c \\ &+ \frac{1}{\sqrt{N}}\sum_{k\omega a}\langle\psi_{k\omega a\alpha}\chi_{p-k,\nu-\omega,a}b^*_{p\nu\alpha}\rangle_c = 1 \end{aligned} \tag{A5}$$

and

$$\begin{aligned} &(i\nu + \lambda)\langle b^*_{-p-\nu-\alpha}b^*_{p\nu\alpha}\rangle_c - 2i\bar{\Delta}\,\text{sgn}(\alpha)\xi_p\langle b_{p\nu\alpha}b^*_{p\nu\alpha}\rangle_c \\ &+ \frac{1}{\sqrt{N}}\sum_{k\omega a}\langle\chi^*_{-p-k,-\nu-\omega,a}\psi^*_{k\omega a,-\alpha}b^*_{p\nu\alpha}\rangle_c = 0, \end{aligned} \tag{A6}$$

where $\langle AB\rangle_c \equiv \langle AB\rangle - \langle A\rangle\langle B\rangle$ is the connected part of correlation function, as indicated by the subscript "c." Note that, in this work, we do not consider the long-range ordered case where $\langle b_{p\nu\alpha}\rangle \neq 0$, we have $\langle AB\rangle_c = \langle AB\rangle$. Similarly, there are two more equations for the off-diagonal correlation function $\langle b_{p\nu\alpha}b_{-p-\nu-\alpha}\rangle_c$, given by the functional derivatives of Eqs. (A3) and (A4) with respect to $I^*_{-p-\nu-\alpha}$.

In the large-N limit, one can safely ignore the vertex corrections since it is subleading [of order of $O(N^{-3/2})$]. Therefore, the three-point correlation functions of Eqs. (A5) and (A6) can be expressed as simple multiplications of the two-point Green's functions:

$$\begin{aligned} \langle\psi_{\boldsymbol{k}\omega a\alpha}\chi_{\boldsymbol{p}-k,\nu-\omega,a}b^*_{\boldsymbol{p}\nu\alpha}\rangle_c &= \frac{1}{\sqrt{N}}G_c(\boldsymbol{k}, i\omega)G_\chi(\boldsymbol{p}-k, i\nu - i\omega)G_b(\boldsymbol{p}, i\nu); \\ \langle\chi^*_{-\boldsymbol{p}-k,-\nu-\omega,a}\psi^*_{\boldsymbol{k}\omega a,-\alpha}b^*_{\boldsymbol{p}\nu\alpha}\rangle_c &= \frac{1}{\sqrt{N}}G_\chi(-\boldsymbol{p}-k, -i\nu - i\omega)G_c(\boldsymbol{k}, i\omega)\langle b^*_{-\boldsymbol{p},-\nu,-\alpha}b^*_{\boldsymbol{p}\nu\alpha}\rangle, \end{aligned} \tag{A7}$$

with

$$\begin{aligned} G_c(\boldsymbol{p}, i\omega) &\equiv -\langle \psi_{\boldsymbol{p}\omega a\alpha} \psi^*_{\boldsymbol{p}\omega a\alpha} \rangle, \\ G_\chi(\boldsymbol{p}, i\omega) &\equiv -\langle \chi_{\boldsymbol{p}\omega a} \chi^*_{\boldsymbol{p}\omega a} \rangle, \\ G_b(\boldsymbol{p}, i\nu) &\equiv -\langle b_{\boldsymbol{p}\nu\alpha} b^*_{\boldsymbol{p}\nu\alpha} \rangle. \end{aligned} \tag{A8}$$

Note that all the Green's function in Eq. (A8) are diagonal in the spin and channel subspaces.

By multiplying both sides of Eq. (A6) with $\mathrm{sgn}(\alpha)$ and defining the α-independent anomalous Green's functions as

$$\begin{aligned} F_b(\boldsymbol{p}, i\nu) &\equiv -\mathrm{sgn}(\alpha) \langle b^*_{-\boldsymbol{p},-\nu,-\alpha} b^*_{\boldsymbol{p}\nu\alpha} \rangle, \\ \bar{F}_b(\boldsymbol{p}, i\nu) &\equiv -\mathrm{sgn}(\alpha) \langle b_{\boldsymbol{p}\nu\alpha} b_{-\boldsymbol{p},-\nu,-\alpha} \rangle, \end{aligned} \tag{A9}$$

one can rewrite Eqs. (A5) and (A6) into the following matrix form:

$$\begin{pmatrix} i\nu - \lambda - \Sigma_b(\boldsymbol{p}, i\nu) & -2i\Delta\xi_{\boldsymbol{p}} \\ 2i\bar{\Delta}\xi_{\boldsymbol{p}} & -i\nu - \lambda - \Sigma_b(-\boldsymbol{p}, -i\nu) \end{pmatrix} \times \begin{pmatrix} G_b(\boldsymbol{p}, i\nu) \\ F_b(\boldsymbol{p}, i\nu) \end{pmatrix} = \begin{pmatrix} 1 \\ 0 \end{pmatrix} \tag{A10}$$

with Σ_b being the self-energy of the b boson, obeying

$$\Sigma_b(\boldsymbol{p}, i\nu) = -\kappa \sum_{\boldsymbol{k}\omega} G_c(\boldsymbol{k} + p, i\omega + i\nu) G_\chi(-\boldsymbol{k}, -i\omega). \tag{A11}$$

The solution of Eq. (A10) can be obtained as

$$\begin{pmatrix} G_b(\boldsymbol{p}, i\nu) \\ F_b(\boldsymbol{p}, i\nu) \end{pmatrix} = \frac{1}{4|\Delta|^2 \xi_{\boldsymbol{p}}^2 - \gamma_b(\boldsymbol{p}, i\nu)\gamma_b(-\boldsymbol{p}, -i\nu)} \times \begin{pmatrix} -\gamma_b(-\boldsymbol{p}, -i\nu) \\ 2i\bar{\Delta}\xi_{\boldsymbol{p}} \end{pmatrix}, \tag{A12}$$

where $\gamma_b(\boldsymbol{p}, i\nu) \equiv i\nu - \lambda - \Sigma_b(\boldsymbol{p}, i\nu)$.

The Dyson-Schwinger equations for $G_c(\boldsymbol{p}, i\omega)$ and $G_\chi(\boldsymbol{p}, i\omega)$ are derived through the same procedure as illustrated above. One has

$$\begin{aligned} G_c^{-1}(\boldsymbol{p}, i\omega) &= i\omega - \varepsilon_{\boldsymbol{p}} - \Sigma_c(\boldsymbol{p}, i\omega), \\ G_\chi^{-1}(\boldsymbol{p}, i\omega) &= -\frac{1}{J_K} - \Sigma_\chi(\boldsymbol{p}, i\omega), \end{aligned} \tag{A13}$$

with the self-energy Σ_c and Σ_χ,

$$\begin{aligned} \Sigma_c(\boldsymbol{p}, i\omega) &= \frac{1}{N} \sum_{k\nu} G_\chi(\boldsymbol{k} - p, i\nu - i\omega) G_b(\boldsymbol{k}, i\nu), \\ \Sigma_\chi(\boldsymbol{p}, i\omega) &= \sum_{\boldsymbol{k},\nu} G_c(\boldsymbol{k} - p, i\nu - i\omega) G_b(\boldsymbol{k}, i\nu). \end{aligned} \tag{A14}$$

As we shall see in Fig. 5 for its diagrammatic representation, $\Sigma_c(\boldsymbol{p}, i\omega)$ is proportional to $1/N$ (each vertex contributes a factor of $1/\sqrt{N}$). In the large-N limit, it is irrelevant as compared with Σ_χ and Σ_b (the diagrammatic representation of Σ_χ and Σ_b is illustrated in Fig. 2). We therefore replace G_c with the bare function $G_{c0}(\boldsymbol{p}, i\omega) = 1/(i\omega - \varepsilon_{\boldsymbol{p}})$ in Eqs. (A11) and (A13).

The variational parameters λ and Δ are obtained via minimizing $\ln Z$ with respect to λ and Δ, i.e., $0 = \partial \ln Z/\partial\lambda = \partial \ln Z/\partial\Delta$, yielding the following self-consistent equations:

$$\begin{aligned} \kappa &= -\sum_{\boldsymbol{p}\nu} G_b(\boldsymbol{p}, i\nu), \\ \frac{1}{J_H} &= -\sum_{\boldsymbol{p}\nu} \frac{\xi_{\boldsymbol{p}}^2}{4|\Delta|^2 \xi_{\boldsymbol{p}}^2 - \gamma_b(\boldsymbol{p}, i\nu)\gamma_b(-\boldsymbol{p}, -i\nu)}. \end{aligned} \tag{A15}$$

For simplicity, we assume all the self-energies are momentum independent. This assumption is widely used in the dynamical mean-field theory approach to the strongly correlated problems. We are thus allowed to integrate Eqs. (A11) to (A15) over the momentum space and take the momentum-independent Green's functions and the self-energies as the unknown variables. We arrive at the following self-consistent equations [with $1/(\beta\mathcal{N}_s)$ recovered] of Eqs. (4)–(6).

APPENDIX B: MOMENTUM AND FREQUENCY SUM

Below, we simplify the momentum sum of the Green's function of spinon G_b of Eq. (4). The momentum sum of G_b can be written as

$$G_b(i\nu) = \frac{-\gamma_b(-i\nu)}{4|\Delta|^2} \frac{1}{\mathcal{N}_s} \sum_{\boldsymbol{p}} \frac{1}{(\sin p_x + \sin p_y)^2 + A}, \tag{B1}$$

where

$$A \equiv -\frac{\gamma_b(i\nu)\gamma_b(-i\nu)}{4|\Delta|^2} \tag{B2}$$

is a momentum-independent complex number. We now take the infinite size limit $\mathcal{N}_s \to \infty$, after which the momentum sum becomes an integral,

$$\begin{aligned} I_1(A) &\equiv \frac{1}{\mathcal{N}_s} \sum_{\boldsymbol{p}} \frac{1}{(\sin p_x + \sin p_y)^2 + A} \\ &= \frac{1}{(2\pi)^2} \int_\Omega \frac{d^2p}{(\sin p_x + \sin p_y)^2 + A} \\ &= \frac{1}{(2\pi)^2} \int_\Omega \frac{d^2p}{A + 4\left(\sin\frac{p_x+p_y}{2} \cos\frac{p_x-p_y}{2}\right)^2} \\ &= \frac{1}{2\pi^2} \int_{x=-\pi}^{\pi} \int_{y=0}^{\pi} \frac{dx\,dy}{A + 4\,\sin^2 x\,\cos^2 y}, \end{aligned} \tag{B3}$$

with Ω being the first Brillouin zone of square lattice. In the last step, we have changed the variables and rearranged the domain of integration, as illustrated in Fig. 7. As one can see, the integrand is divergent within the range $-4 < A < 0$.

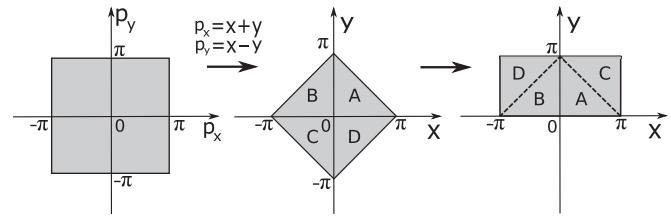

FIG. 7. Rearrangement of the momentum integration domain.

Outside this range, the integral can be performed as

$$I_1(A) = \frac{2}{\pi A}\int_0^{\pi/2} dx \frac{1}{\sqrt{1+\frac{4}{A}\sin^2 x}} = \frac{2}{\pi A} E_K\left[-\frac{4}{A}\right], \quad \text{(B4)}$$

where $E_K[Z]$ is the complete elliptic integral of the first kind (elliptic-K function). The function $E_K[Z]$ is analytic in the whole complex plane except for a branch cut along the real axis $\mathrm{Re}Z > 1$, which exactly corresponds to the range $-4 < A < 0$ for $Z = -4/A$. Substituting this result into Eq. (B1), one obtains

$$G_b(i\nu) = \frac{2}{\pi\gamma_b(i\nu)} E_K\left[\frac{16|\Delta|^2}{\gamma_b(i\nu)\gamma_b(-i\nu)}\right]. \quad \text{(B5)}$$

It is useful to rewrite the momentum integral as

$$I_1(A) \equiv \int_0^4 d\varepsilon \frac{\rho(\varepsilon)}{\varepsilon + A} = \frac{2}{\pi A} E_K\left[-\frac{4}{A}\right], \quad \text{(B6)}$$

where

$$\rho(\varepsilon) = \frac{1}{\mathcal{N}_s}\sum_p \delta(\varepsilon - (\sin p_x + \sin p_y)^2) \quad \text{(B7)}$$

is the density of states of the free spinon.

Following a similar approach, one can further simplify the momentum sum of the self-consistent equation for Δ in Eq. (6). We first introduce the following function I_2, given by

$$\begin{aligned} I_2(A) &\equiv \frac{1}{\mathcal{N}_s}\sum_p \frac{(\sin p_x + \sin p_y)^2}{(\sin p_x + \sin p_y)^2 + A} = \int_0^4 d\varepsilon \frac{\varepsilon\rho(\varepsilon)}{\varepsilon + A} \\ &= \int_0^4 d\varepsilon\, \rho(\varepsilon) - A\int_0^4 d\varepsilon \frac{\rho(\varepsilon)}{\varepsilon + A} \\ &= 1 - \frac{2}{\pi} E_K\left[-\frac{4}{A}\right]. \end{aligned} \quad \text{(B8)}$$

Therefore, the second equation in Eq. (6) takes the form

$$\begin{aligned} \frac{1}{J_H} &= -\frac{1}{4|\Delta|^2\beta}\sum_\nu I_2\left(-\frac{\gamma_b(i\nu)\gamma_b(-i\nu)}{4|\Delta|^2}\right) \\ &= \frac{1}{2\pi|\Delta|^2}\int_{-\infty}^{\infty}\frac{d\nu}{\pi}\frac{1}{e^{\beta\nu}-1} \\ &\quad \times \mathrm{Im}E_K\left[\frac{16|\Delta|^2}{\gamma_b(\nu+i0^+)\gamma_b(-\nu+i0^+)^*}\right], \end{aligned} \quad \text{(B9)}$$

where the Matsubara sum is transformed into an integration according to the formula ($\eta = \pm 1$ for fermion and boson, respectively):

$$\frac{1}{\beta}\sum_{\omega_n} F(\omega_n) e^{i\omega_n 0^+} = \int_{-\infty}^{\infty}\frac{d\omega}{\pi}\frac{-\eta}{e^{\beta\omega}+\eta}\mathrm{Im}F(\omega + i0^+). \quad \text{(B10)}$$

Similarly one has, for the other constraint,

$$\kappa = -\frac{1}{\beta}\sum_\nu G_b(i\nu) = -\int_{-\infty}^{\infty}\frac{d\nu}{\pi}\frac{1}{e^{\beta\nu}-1}\mathrm{Im}G_b(\nu + i0^+). \quad \text{(B11)}$$

The frequency sums in the self-energies of Eq. (5) can be performed using the usual Matsubara technique as follows:

$$\begin{aligned} \Sigma_\chi(i\omega) &= -\sum_{z_0}\mathrm{Res}\left[\frac{1}{e^{\beta z}-1}G_{c0}(z - i\omega)G_b(z)\right] \\ &= \int\frac{dx}{\pi}\left[\frac{1}{e^{\beta x}-1}G_{c0}(x - i\omega)\mathrm{Im}G_b(x)\right. \\ &\quad \left. -\frac{1}{e^{\beta x}+1}G_b(x + i\omega)\mathrm{Im}G_{c0}(x)\right], \end{aligned} \quad \text{(B12)}$$

where z_0 denotes the poles of $G_{c0}G_b$ in the first line of the above equation. Following a similar approach, Σ_b can be obtained as

$$\begin{aligned} \Sigma_b(i\nu) = -\kappa\int\frac{dx}{\pi}&\left[\frac{1}{e^{-\beta x}+1}G_{c0}(i\nu - x)\mathrm{Im}G_\chi(x)\right. \\ &\left. -\frac{1}{e^{\beta x}+1}G_\chi(i\nu - x)\mathrm{Im}G_{c0}(x)\right]. \end{aligned} \quad \text{(B13)}$$

APPENDIX C: SPECTRAL FUNCTIONS AND ANTIFERROMAGNETIC LONG-RANGE ORDER

The Green's functions can be obtained by solving the self-consistent equations numerically. Due to the branch cut of the elliptic-K function (E_K) in G_b, the spinon spectral function develops discontinuity within some region of the parameter spaces. We now show that this discontinuity corresponds to the development of antiferromagnetic long-range order (AF LRO). The branch cut of elliptic-K function lies at the real axis of its complex argument, running from 1 to infinity, indicated as the black solid line in Fig. 8(a). For comparison, let us first consider the pure 2D Heisenberg model ($J_K = 0$), in which the argument of the elliptic-K function can be simplified as $Z = 16|\Delta|^2/(\lambda^2 - \nu^2 - 2i\nu\delta)$. For different values of $\lambda^2/16|\Delta|^2$, the function $Z(\nu)$ intersects with the real axis at different positions. For $\lambda^2 < 16|\Delta|^2$, $Z(\nu)$ intersects with the branch cut, resulting in a discontinuity of the spinon spectral function [Fig. 8(b)]. Right at $\lambda^2 = 16|\Delta|^2$, the spectral function has a finite value at zero frequency, corresponding to massless Goldstone mode associated with the formation of AF LRO.

According to the Mermin-Wagner theorem, AF LRO in the 2D Heisenberg model is always destroyed by fluctuations at any finite temperatures. This can be confirmed by solving the two self-consistent equations of Eq. (6) in the Heisenberg limit (or, equivalently, in the absence of the self-energy Σ_b of Schwinger bosons which is generated by the Kondo term). In the Heisenberg limit and for $\kappa \geqslant 0.2$, the spinon gap $\lambda - 4|\Delta|$ always remains positive down to the lowest temperatures we can reach [see Fig. 8(c)] and tends to vanish at $T = 0$, thus rules out the formation of finite-temperature AF-LRO state. We further found that the temperature-dependent spinon gap at the low-temperature regime obeys the analytical result of the large-N [SU(N)] Schwinger-boson approach to the 2D antiferromagnetic Heisenberg in Refs. [32,36], i.e., $\lambda(T) - 4\Delta(T) = (a/T)\exp(-b/T)$ where the constants $a, b \propto JSZ_c$ with J being the antiferromagnetic coupling, S being the effective spin, and Z_c being the renormalization factor of spin-wave velocity [see the black dashed lines in

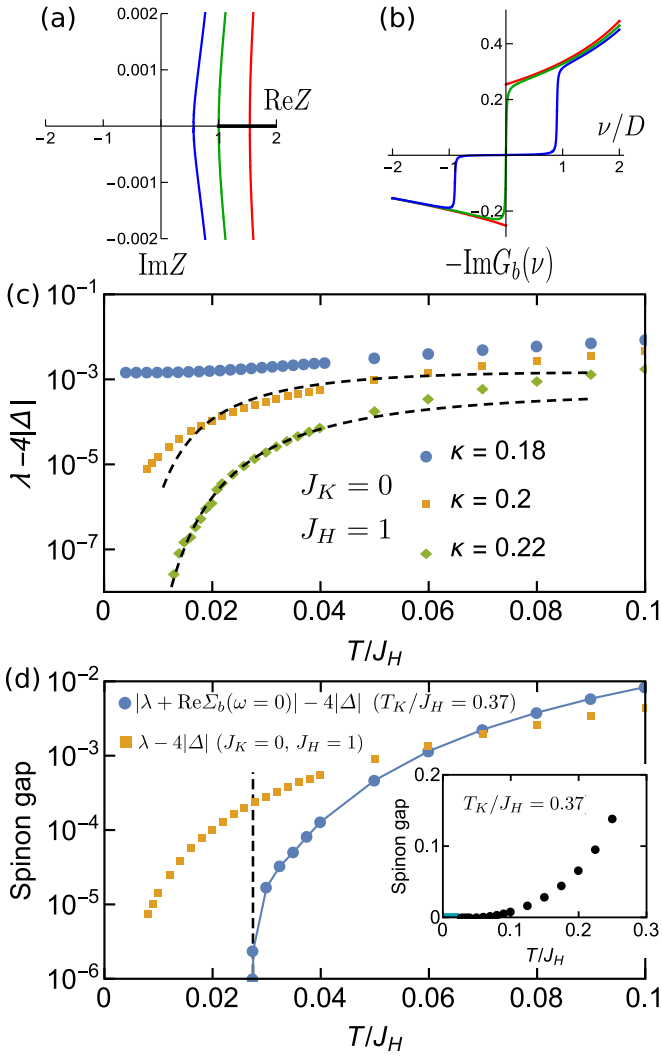

FIG. 8. (a) Branch cut of elliptic-K function on the complex Z plane, indicated as the black solid line. For a pure Heisenberg model ($J_K=0$), one has $Z=16|\Delta|^2/(\lambda^2-\nu^2-2i\nu\delta)$. The three curves show evolution of Z upon varying frequencies in three different cases: $\lambda^2>,=,<16|\Delta|^2$. (b) The corresponding spinon spectral function of the 2D Heisenberg model. (c) Spinon gap $\lambda-4\Delta$ of the pure Heisenberg model with $\kappa=0.18$ (blue), $\kappa=0.2$ (orange), and $\kappa=0.22$ (green). The black dashed lines represent fitting to $(a/T)\exp(-b/T)$ with a, b being fitting parameters. No finite-temperature AF LRO (corresponding to $\lambda-4|\Delta|=0$) can be found down to the lowest temperatures. (d) Spinon gaps of the pure Heisenberg model with $\kappa=0.2$ (orange) and the Kondo-Heisenberg model $|\lambda+\mathrm{Re}\Sigma_b(\omega=0)|-4|\Delta|$ with $T_K/J_H=0.37$ with $\kappa=0.2$ (blue). The black dashed line marks the temperature at which the 2D Kondo-Heisenberg model (with $\kappa=0.2$, $T_K/J_H=0.37$) starts to form AF LRO, corresponding to the condition $|\lambda+\mathrm{Re}\Sigma_b(i0^+)|-4|\Delta|=0$. Inset of (b): spinon gap of the Kondo-Heisenberg model in the linear-linear scale. The thick blue line indicates the temperature range where the spinon gap vanishes.

Fig. 8(c)]. Therefore, our results in the Heisenberg limit obey the Mermin-Wagner theorem.

However, in the more general case 2D Kondo-Heisenberg model ($J_K\neq 0$), the AF-LRO state at finite temperatures

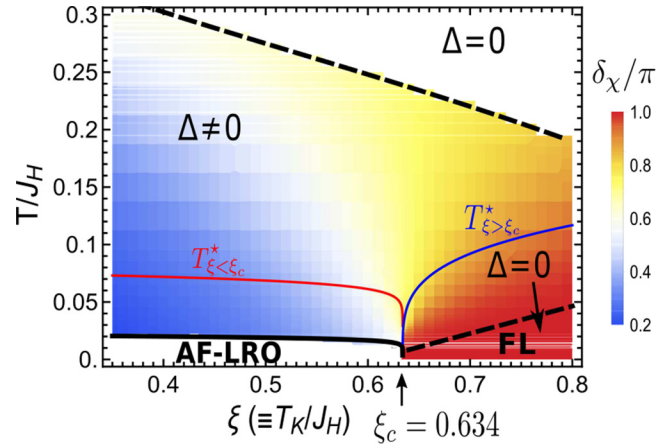

FIG. 9. Finite-temperature phase diagram of the 2D Kondo-Heisenberg model, determined by the value of holon phase shift δ_χ/π. The red and blue curves marked as $T^\star_{\xi<\xi_c}$ and $T^\star_{\xi>\xi_c}$ are the characteristic temperatures above which the local magnetic susceptibility shows quantum critical scaling.

indeed violates the Mermin-Wagner theorem within our approach. This needs further investigations. When considering the Kondo coupling, the corresponding condition for the formation of AF LRO is modified as $|\lambda+\mathrm{Re}\Sigma_b(i0^+)|-4|\Delta|=0$. This can be deduced by combining

$$\mathrm{Re}\left[\frac{16|\Delta|^2}{\gamma_b(\nu+i0^+)\gamma_b(-\nu+i0^+)^*}\right]\Bigg|_{\nu=0}\geqslant 1 \qquad \text{(C1)}$$

with the fact that $\mathrm{Im}\Sigma_b(i0^+)=0$ [see Eq. (B13)]. Our numerical result shows that the spinon gap $|\lambda+\mathrm{Re}\Sigma_b(i0^+)|-4|\Delta|$ indeed vanishes below a particular finite temperature [see Fig. 8(d)]. We think that it is the $\mathrm{Re}\Sigma_b(i0^+)$ term that tends to cancel the contributions from $\lambda-4\Delta$, making the spinon dispersion gapless at finite temperatures. We therefore tend to conclude that the self-energy of Schwinger boson, Σ_b, is responsible for the formation of AF LRO, which indirectly implies that the emergence of AF LRO is primarily due to the Kondo term [see Fig. 8(d)]. To further check what causes the cancellation of the spinon gap mentioned above, one of our coauthors and his collaborators generalized our approach to include momentum dependence in Σ_b in the KH model. They showed that the finite-temperature AF-LRO region disappears as the spinon gap remains finite at finite temperatures. They further showed a power-law divergence in staggered magnetic susceptibility on the AF side, extending to $T\ll T_{\mathrm{LRO}}$ [45]. The above reasons/findings strongly suggest that the violation of Mermin-Wagner theorem in our finite-temperature AF-LRO phase when $J_K\neq 0$, $J_H\neq 0$ is likely due to the neglect of momentum dependence in the self-energies. We think that neglecting the momentum- dependent self-energies may simultaneously make us neglect the effect of long-wavelength spin fluctuations of the RKKY interaction induced by Kondo coupling, which, via the Mermin-Wagner theorem, is responsible for destroying the magnetic order in low-dimensional systems. This will lead to the formation of AF-LRO state at finite temperatures as we show in our finite-temperature phase diagram.

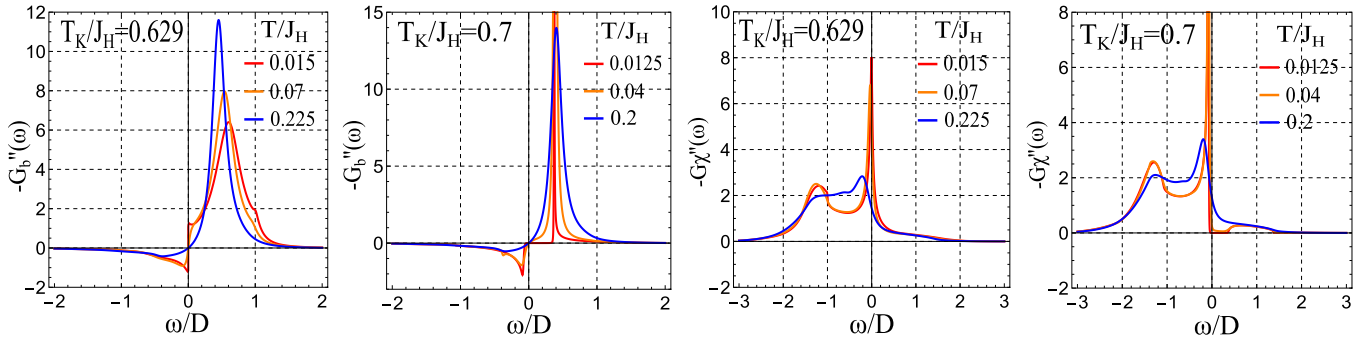

FIG. 10. Holon and spinon spectral functions for the 2D Kondo-Heisenberg lattice model at different sides of the QCP ($T_K/J_H = 0.629$ and $T_K/J_H = 0.7$, respectively). The spinon spectral function at $T_K/J_H = 0.629$ shows appearance of zero-energy mode at $T/J_H = 0.015$ (red curve). Both spinon and holon develop gaps at the Kondo side.

Figure 9 shows the full phase diagram in the $T/J_H \sim T_K/J_H$ plane, determined by the value of holon phase shift $\delta_\chi = -\mathrm{Im}\ln[1 + J_K\Sigma_\chi(i0^+)]$. Note that the conduction electron phase shift δ_c (per spin flavor per screening channel) is related to the holon phase shift via the Ward identity $\delta_c = \delta_\chi/N$, producing in total an order $O(N \times K/N) = O(N)$ contribution to free energy (see Ref. [28]). The phase boundary of AF LRO (the black solid curve) is determined by the condition $|\lambda + \mathrm{Re}\Sigma_b(i0^+)| - 4|\Delta| = 0$. Figures 10 and 11 show evolution of spinon and holon spectral functions of the 2D Kondo-Heisenberg model on varying temperatures and T_K/J_H, respectively. In Figs. 11(a) and 11(b), we observe a slight shift of the peak position of the holon spectrum $-G''_\chi(\omega)$ as one moves across the QCP [see the black areas in Figs. 11(a) and 11(b)]. Figure 12 shows the imaginary part of the conduction-electron self-energies, $-\mathrm{Im}\Sigma_c(\omega)$, and its spectral functions, $-\mathrm{Im}G_c(k,\omega)$, calculated at finite$-N$. In Fig. 12(a), we find the absence of the Kondo resonance peak at the Fermi energy, due to an artifact of our approach. Fig. 12(c) reveals a Fermi surface enlargement as T_K/J_H is tuned to the Fermi liquid regime.

APPENDIX D: CONDUCTION ELECTRON T MATRIX

To check the Kondo resonance peak on the paramagnetic phase, we further calculate the conduction electron T matrix, defined as

$$T(\omega) = \frac{\Sigma_c(\omega)}{1 - G_{c0}(\omega)\Sigma_c(\omega)}. \tag{D1}$$

We find that the imaginary part of the T matrix at the large-N level vanishes near the Fermi energy, while it shows a resonance peak at an energy of the order of the holon gap ($\sim T_K$). The absence of the Kondo resonance peak at the Fermi energy is due to the holon and spinon gaps of order T_K, and is an artifact of the Schwinger-boson approach. As is shown in Ref. [33], including $1/N$ corrections, e.g., through a fully self-consistent evaluation results in a gapless T matrix where the peak position of the resonance is identical to that at the large-N level. Figure 13 shows the temperature evolution of the T matrix with the following choice of parameters: $N = 10$, $K = 2$, $T_K/D = 0.082$, $T_K/J_H = 0.852$. The value at zero energy appears to saturate at low temperatures and agrees reasonably well with the Friedel sum rule

$$-\pi\rho\,\mathrm{Im}T(0 + i\eta) = \sin^2\delta_c, \tag{D2}$$

where $\delta_c = \delta_\chi/N = \pi/N$ is the electron phase shift at zero temperature when the impurities are exactly screened. Similar results have been obtained for the Schwinger-boson approach to the infinite-U single-impurity Anderson model (see Ref. [33]).

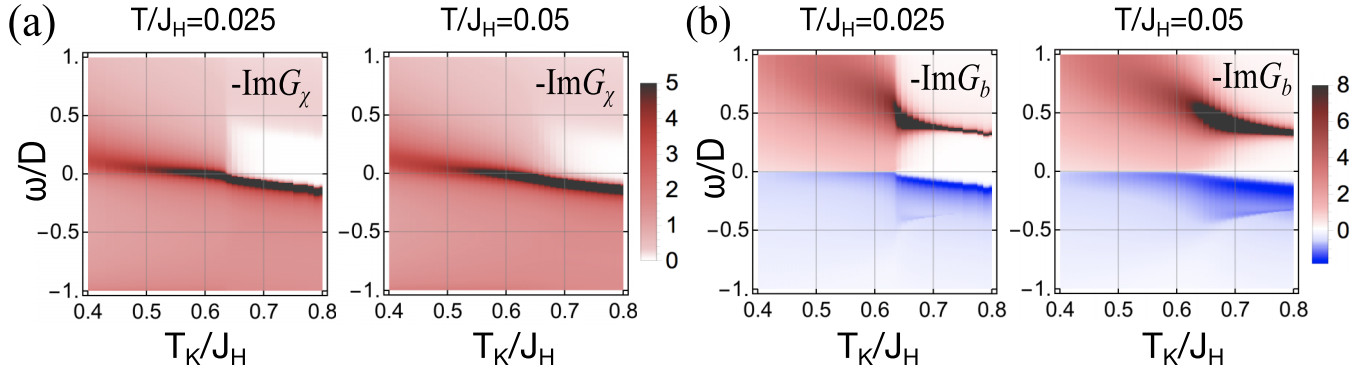

FIG. 11. Density plots of (a) holon and (b) spinon spectral functions at $T/J_H = 0.025$ and $T/J_H = 0.05$, respectively.

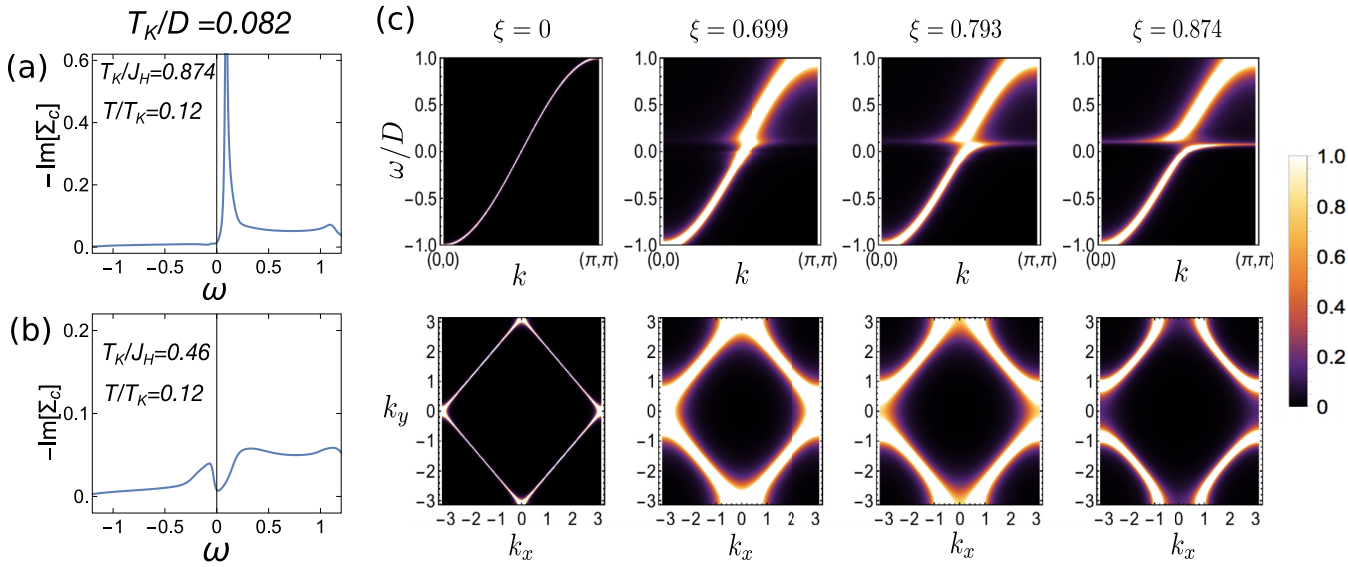

FIG. 12. (a), (b) Imaginary part of conduction electron self-energy at $T_K/D = 0.082$, and for different values of T_K/J_H. (c) Spectral function of the c electrons, $-\mathrm{Im}G_c(k,\omega)$, and the corresponding Fermi surface, $-\mathrm{Im}G_c(k_x,k_y,\omega=0)$. We take $N = 10$ here. In the upper row of (c), the spectral functions are plotted along $k \equiv \sqrt{k_x^2+k_y^2}$ for $k_x = k_y$, in between $(k_x,k_y) = (0,0)$ and (π,π) of the first Brillouin zone.

APPENDIX E: MAGNETIC SUSCEPTIBILITY

To derive the static magnetic susceptibility, we add the following source term to the action:

$$S_{\mathrm{zee}} = -\sum_{i\nu\alpha} H_i \,\mathrm{sgn}(\alpha) b^*_{i\nu\alpha} b_{i\nu\alpha}, \tag{E1}$$

where S_{zee} is along the z direction and H_i can be interpreted as the magnitude of perpendicular magnetic field at site i. We consider the direction of the sublattice magnetization is parallel to S_{zee}, thus has the form

$$M_i = \frac{d\,\ln Z}{dH_i} = \sum_{\nu\alpha} \mathrm{sgn}(\alpha) b^*_{i\nu\alpha} b_{i\nu\alpha}, \tag{E2}$$

where we have dropped the notations for the orientation of M_i and S_{zee} throughout this paper. The magnetic susceptibility $\chi_{\mathrm{ij}} \equiv dM_i/dH_j$ is given by

$$\begin{aligned}\chi_{\mathrm{ij}} &= \langle M_i M_j\rangle - \langle M_i\rangle\langle M_j\rangle \\ &= \sum_{\nu\alpha\nu'\alpha'} \mathrm{sgn}(\alpha)\mathrm{sgn}(\alpha')[\langle b^*_{i\nu\alpha} b_{i\nu\alpha} b^*_{j\nu'\alpha'} b_{j\nu'\alpha'}\rangle \\ &\quad -\langle b^*_{i\nu\alpha} b_{i\nu\alpha}\rangle\langle b^*_{i\nu'\alpha'} b_{i\nu'\alpha'}\rangle].\end{aligned} \tag{E3}$$

Since we are not considering the LRO phase, M_i vanishes without external magnetic field. One therefore has

$$\begin{aligned}\chi_{\mathrm{ij}} &= \sum_{\nu,\alpha;\nu',\alpha'} \mathrm{sgn}(\alpha)\mathrm{sgn}(\alpha')\{\langle b_{j\nu'\alpha'} b^*_{i\nu\alpha}\rangle\langle b_{i\nu\alpha} b^*_{j\nu'\alpha'}\rangle + \langle b^*_{i\nu\alpha} b^*_{j\nu'\alpha'}\rangle\langle b_{i\nu\alpha} b_{j\nu'\alpha'}\rangle\} \\ &= \frac{1}{\beta\mathcal{N}_s^2}\sum_{\boldsymbol{p},k,\nu,\alpha}[G_b(\boldsymbol{p},i\nu)G_b(\boldsymbol{k},i\nu) - F_b(\boldsymbol{p},i\nu)\bar{F}_b(\boldsymbol{k},i\nu)]e^{i(\boldsymbol{k}-p)\cdot(r_i-r_j)} = \chi_{i-j}.\end{aligned} \tag{E4}$$

The local susceptibility is defined as

$$\frac{\chi_{\mathrm{loc}}}{N} \equiv \frac{\chi_{i-j=0}}{N} = \frac{1}{\beta}\sum_{\nu} G_b(i\nu)G_b(i\nu).$$

Here the anomalous function has no contribution since $\sum_p F_b(p,i\nu) = 0$. However, it contributes to the uniform susceptibility

$$\begin{aligned}\frac{\chi_{\mathrm{uni}}}{N} \equiv \sum_{i-j}\frac{\chi_{i-j}}{N} &= \frac{1}{\beta\mathcal{N}_s}\sum_{\boldsymbol{p},\nu}[G_b(\boldsymbol{p},i\nu)G_b(\boldsymbol{p},i\nu) \\ &\quad - F_b(\boldsymbol{p},i\nu)\bar{F}_b(\boldsymbol{p},i\nu)].\end{aligned} \tag{E5}$$

The momentum sum can be performed using the previous results (B6) and (B7) as

$$\begin{aligned}&\frac{1}{\mathcal{N}_s}\sum_{\boldsymbol{p}} G_b(\boldsymbol{p},i\nu)G_b(\boldsymbol{p},i\nu) \\ &= \frac{\gamma_b(-i\nu)^2}{16|\Delta|^4}\frac{1}{\mathcal{N}_s}\sum_{\boldsymbol{p}}\frac{1}{[(\sin p_x+\sin p_y)^2+A]^2} \\ &= \frac{\gamma_b(-i\nu)^2}{16|\Delta|^4}\int_0^4 d\varepsilon\frac{\rho(\varepsilon)}{(\varepsilon+A)^2} \\ &= -\frac{\gamma_b(-i\nu)^2}{16|\Delta|^4}\frac{\partial I_1(A)}{\partial A}\end{aligned} \tag{E6}$$

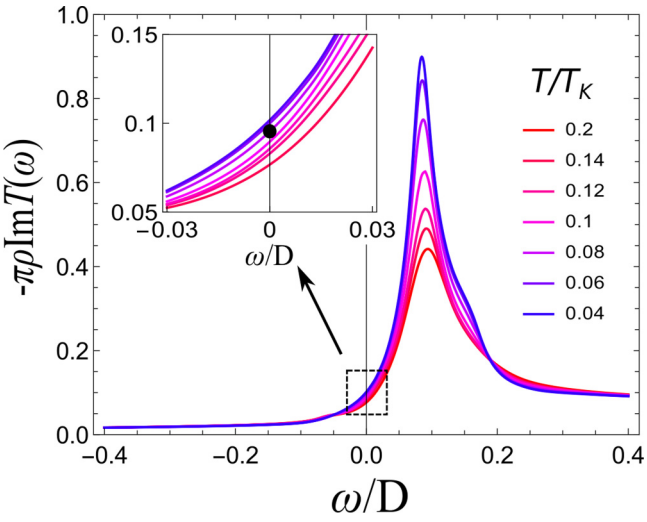

FIG. 13. The imaginary part of scattering T matrix $T(\omega)$, obtained by solving the self-consistent equations at finite N with the following choice of parameters: $N = 10$, $K = 2$, $T_K/D = 0.082$, $T_K/J_H = 0.852$. The inset shows the region near the Fermi energy, where the black dot marks the value $\sin^2(\pi/N)$.

and

$$\frac{1}{\mathcal{N}_s}\sum_{\boldsymbol{p}} F_b(\boldsymbol{p}, i\nu)\bar{F}_b(\boldsymbol{p}, i\nu)$$
$$= \frac{1}{4|\Delta|^2}\frac{1}{\mathcal{N}_s}\sum_{\boldsymbol{p}}\frac{(\sin p_x + \sin p_y)^2}{[(\sin p_x + \sin p_y)^2 + A]^2}$$
$$= \frac{1}{4|\Delta|^2}\int_0^4 d\varepsilon \frac{\varepsilon\rho(\varepsilon)}{(\varepsilon + A)^2}$$
$$= -\frac{1}{4|\Delta|^2}\frac{\partial I_2(A)}{\partial A}. \tag{E7}$$

According to the following identity,

$$\frac{\partial}{\partial z}E_K[z] = \frac{E_E[z] - (1-z)E_K[z]}{2z(1-z)}, \tag{E8}$$

where $E_E(z) = \int_0^{\pi/2}\sqrt{1 - z\sin^2\theta}\, d\theta$, one has

$$\frac{\chi_{\rm uni}}{N} = \frac{1}{\pi\beta}\sum_{\nu}\left(\frac{\gamma_b(i\nu) - \gamma_b(-i\nu)}{4|\Delta|^2\gamma_b(i\nu)}\frac{E_E\left[\frac{-4}{A}\right]}{4 + A}\right.$$
$$\left. + \frac{\gamma_b^{-1}(i\nu) + \gamma_b^{-1}(-i\nu)}{\gamma_b(i\nu)}E_K\left[\frac{-4}{A}\right]\right). \tag{E9}$$

The results for uniform susceptibility $\chi_{\rm uni}(T)$ are shown in Fig. 14(a). The temperature dependence of uniform susceptibility at $\xi = 0.95$ is consistent with what one would expect, i.e., $\chi_{\rm uni}(T)$ exhibits a $1/T$ Curie law at high temperatures [see Fig. 14(c)] and reaches a saturated value at low temperatures when the local moments are completely screened. As T_K/J_H approaches the QCP, the uniform susceptibility is suppressed at intermediate temperatures. This is caused by the nonzero value of RVB mean-field value Δ in this region.

Here, we give evidences for its critical scaling behaviors in different regions of the phase diagram. One of the scaling

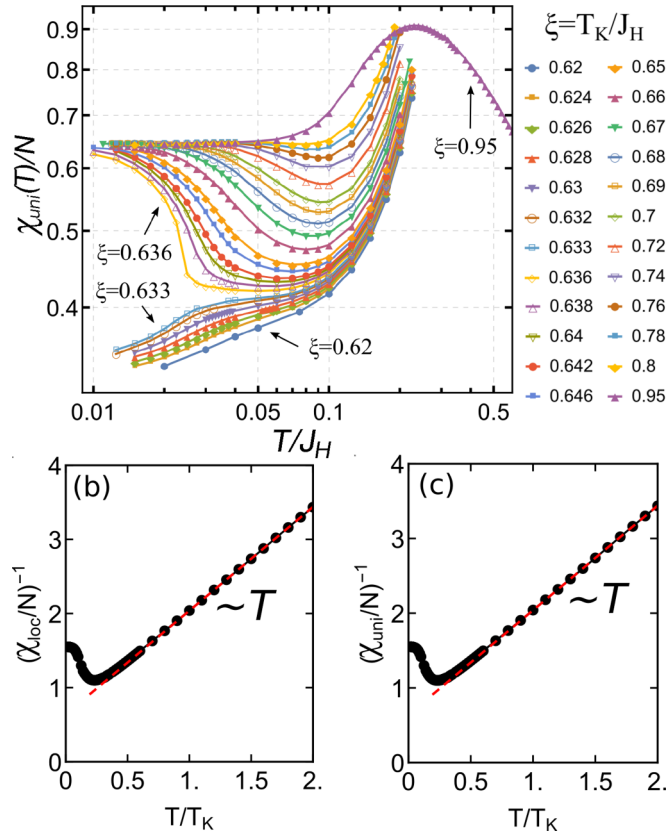

FIG. 14. (a) Uniform magnetic susceptibility at different values of $\xi = T_K/J_H$. The inverse (b) local and (c) uniform spin susceptibility for $T_K/J_H = 0.95$. Both $\chi_{\rm loc}$ and $\chi_{\rm uni}$ show $1/T$ Curie-law behavior at higher temperatures, as indicated by the red dashed lines.

behaviors is the power-law scaling right above the antiferromagnetic LRO boundary, with a characteristic temperature proportional to the "Néel temperature" of the AF-LRO phase denoted by T_1^* [see Fig. 15(a)]. Another scaling behavior is the quantum critical scaling in the region above the two crossover temperatures $T^\star_{\xi<\xi_c}$ and $T^\star_{\xi>\xi_c}$ (see the red and blue curves in Fig. 9) [$T^\star_{\xi<\xi_c}$ and $T^\star_{\xi>\xi_c}$ exhibit a power-law behavior with $|\xi - \xi_c|$, see the right panel of Fig. 15(c)]. Figure 15(b) shows the collapsed data in the quantum critical region, exhibiting a possible power-law scaling with the exponents α varying linearly with ξ [see the left panel of Fig. 15(c)].

In addition, we also estimate the behavior of both $\chi_{\rm loc}$ and $\chi_{\rm uni}$ in the AF-LRO phase $T \leqslant T_{\rm LRO}$ where the boson condensate is developed, i.e., $x_{i\alpha} \equiv \langle b_{i\nu\alpha}\rangle \neq 0$. This estimation is shown below: we start from the general expression of spin susceptibility of Eq. (E3). For temperatures below the LRO-AF transition temperature, to include the boson condensate we need to rewrite a boson operator b as its mean-field condensate value x plus its fluctuation δb: $b_{i\nu\alpha} = x_{i\alpha} + \delta b_{i\nu\alpha}$. Note that $b_{i\nu\alpha} = \delta b_{i\nu\alpha}$ if there is no condensate. For $x \neq 0$, the general expression of spin susceptibility of Eq. (E3) can be proved as

$$\chi_{\rm ij} = \sum_{\nu\nu'\alpha\alpha'}{\rm sgn}(\alpha){\rm sgn}(\alpha')[\langle b_{j\nu'\alpha'}b^*_{i\nu\alpha}\rangle_c\langle b_{i\nu\alpha}b^*_{j\nu'\alpha'}\rangle_c$$
$$+ \langle b^*_{i\nu\alpha}b^*_{j\nu'\alpha'}\rangle_c\langle b_{i\nu\alpha}b_{j\nu'\alpha'}\rangle_c], \tag{E10}$$

where $\langle\ldots\rangle_c$ denotes connected correlation function. In deriving Eq. (E10), we neglect the three- and four-boson correlators

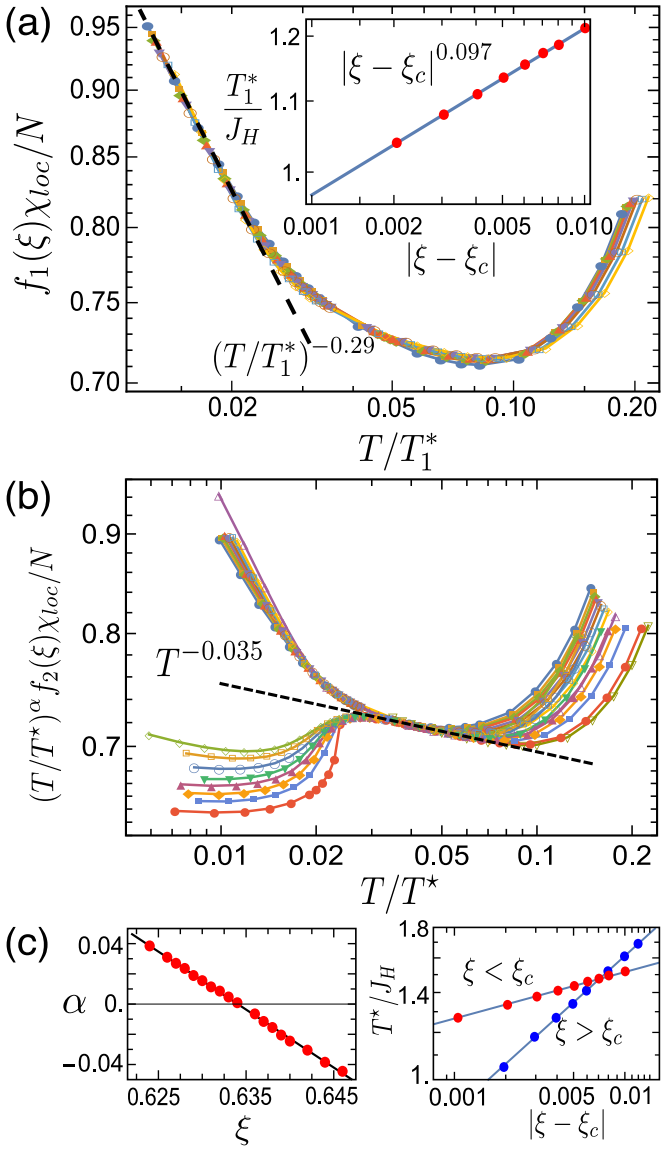

FIG. 15. Critical scaling of local susceptibility in (a) the region above the antiferromagnetic-LRO phase, and (b) the quantum critical region. Here, T_1^* is proportional to the "Néel temperature" of the AF-LRO phase, $T^\star$ is the crossover temperature to the quantum critical region which shows different power-law behavior for $\xi > \xi_c$ and $\xi < \xi_c$ [see Fig. 9 and (c) below], and α is a nonuniversal exponent [see (c) below]. (c) Right: $T^\star/J_H$ versus $|\xi - \xi_c|$ for $\xi > \xi_c$ (blue) and $|\xi - \xi_c|$ (red), respectively. Left: α versus ξ.

and use the following identities of the four- and two-boson correlators:

$$\begin{aligned}\langle ABCD\rangle =& \langle A\rangle\langle B\rangle\langle C\rangle\langle D\rangle + \langle A\rangle\langle BCD\rangle_c + \langle B\rangle\langle ACD\rangle_c \\ &+ \langle C\rangle\langle ABD\rangle_c + \langle D\rangle\langle ABC\rangle_c + \langle AB\rangle_c\langle CD\rangle_c \\ &+ \langle AC\rangle_c\langle BD\rangle_c + \langle AD\rangle_c\langle BC\rangle_c + \langle ABCD\rangle \quad \text{(E11)}\end{aligned}$$

and

$$\begin{aligned}&\langle AB\rangle = \langle A\rangle\langle B\rangle + \langle AB\rangle_c \\ &\Rightarrow \langle AB\rangle_c = \langle (A-\langle A\rangle)(B-\langle B\rangle)\rangle = \langle \delta A \delta B\rangle \quad \text{(E12)}\end{aligned}$$

with A, B, C, D in Eqs. (E11) and (E12) being boson operators and δA and δB being the fluctuations of A and B. In the absence of boson condensation $\langle A\rangle = \langle B\rangle = 0$, we have $\langle AB\rangle = \langle AB\rangle_c$ and Eq. (E10) goes back to Eq. (E4). Via Eq. (E12), it is easy to see that the spin susceptibility of Eq. (E10) only explicitly depends on the fluctuations of Schwinger boson.

As Eq. (E10) only depends on fluctuations, it suggests the spin susceptibility reaches its maxima at the transition temperature $T_{\rm LRO}$ where the fluctuations of boson prevail. As temperature is lower than $T_{\rm LRO}$, the boson fluctuations tend to be suppressed as the strength of the boson condensate gets enhanced with decreasing of temperature, giving rise to a monotonic decrease of spin susceptibility. Eventually, it approaches the minima at $T = 0$ where the boson condensation is completely developed. Alternatively, the vanishing of spin susceptibility at $T = 0$ can be simply obtained from Eqs. (11) and (E3). See Sec. IV C for details. We prove that both $\chi_{\rm loc}$ and $\chi_{\rm uni}$ maximize at $T = T_{\rm LRO}$ and, as the system enters the LRO phase, start to decrease as the condensation of bosons becomes more dominant with the decreasing of temperature. Both the local and uniform spin susceptibilities eventually vanish as $T \to 0$.

APPENDIX F: ENTROPY

Here, we simplify the expression of entropy, Eq. (8). The momentum sum in Eq. (8) can be performed as

$$\begin{aligned}&\frac{1}{N_s}\sum_{\boldsymbol{p}} \ln\left[\det\left\{-\mathbf{G}_b^{-1}(\boldsymbol{p},\nu)\right\}\right] \\ &= \frac{1}{N_s}\sum_{\boldsymbol{p}} \ln\left[\gamma_b(\nu)\gamma_b(-\nu) - 4|\Delta|^2\xi_{\boldsymbol{p}}^2\right] \\ &= \ln(-4|\Delta|^2) + \frac{1}{N_s}\sum_{\boldsymbol{p}} \ln\left(\xi_{\boldsymbol{p}}^2 + A\right), \quad \text{(F1)}\end{aligned}$$

and using the density of states defined in Eq. (B7), we have

$$\frac{1}{N_s}\sum_{p} \ln\left(\xi_p^2 + A\right) = \int_0^4 d\varepsilon\, \rho(\varepsilon)\ln(\varepsilon + A). \quad \text{(F2)}$$

Noticing that

$$\frac{\partial}{\partial A}\int_0^4 d\varepsilon\, \rho(\varepsilon)\ln[\varepsilon + A] = \int_0^4 d\varepsilon \frac{\rho(\varepsilon)}{\varepsilon + A} = \frac{2}{\pi A}E_K\left[-\frac{4}{A}\right], \quad \text{(F3)}$$

one can first assume A is real and perform the integration over A,

$$\begin{aligned}\int_0^4 d\varepsilon\, \rho(\varepsilon)\ln[\varepsilon + A] =& \frac{2}{\pi}\int \frac{dA}{A}E_K\left[-\frac{4}{A}\right] \\ =& \frac{1}{\pi}G_{3,3}^{2,2}\left(\frac{4}{A}\middle| \begin{matrix}1/2, 1/2, 1\\ 0, 0, 0\end{matrix}\right) + C. \quad \text{(F4)}\end{aligned}$$

Here, $G_{3,3}^{2,2}(\frac{4}{A}|\begin{smallmatrix}\frac{1}{2},\frac{1}{2},1\\0,0,0\end{smallmatrix})$ is the Meijer G function, and C is a constant independent of A. Since $\lim_{A\to 0} G_{3,3}^{2,2}(\frac{4}{A}|\begin{smallmatrix}\frac{1}{2},\frac{1}{2},1\\0,0,0\end{smallmatrix}) = 0$, one

has

$$C = \int_0^4 d\varepsilon\, \rho(\varepsilon) \ln \varepsilon = \frac{1}{\mathcal{N}_s} \sum_{\boldsymbol{p}} \ln[(\sin p_x + \sin p_y)^2]$$
$$= \frac{1}{(2\pi)^2} \int_\Omega d^2p\, \ln\left[4\left(\sin\frac{p_x+p_y}{2}\cos\frac{p_x-p_y}{2}\right)^2\right]$$
$$= \frac{1}{2\pi^2} \int_{x=-\pi}^{\pi} \int_{y=0}^{\pi} \ln[4\sin^2 x \cos^2 y] = -2\ln 2. \quad \text{(F5)}$$

The result is then analytically continued to the whole complex-A plane. The other terms in Eq. (8) are independent of momentum.

APPENDIX G: FINITE-N CALCULATIONS

In this Appendix, we summarize the results of the self-consistent Schwinger-Dyson equations for the Kondo-Heisenberg model with the inclusion of finite N ($N = 10,\ 20$) correction.

Finite-temperature phase diagram. The finite-temperature phase diagram with finite value of N ($N = 10$) in terms of the dimensionless tuning parameter $\xi \equiv T_K/J_H$ and temperature T/J_H is mapped out via the specific-heat coefficient C_V/NT, as shown in Fig. 6 in Sec. V. At zero temperature, a QCP at $\xi = \xi_c \approx 0.517$, separating the AF-LRO phase at small ξ and the paramagnetic FL ground state at large ξ is clearly identified via the low-temperature evolution of various quantities. The observed phases and features including a AF-LRO state at $\xi < \xi_c$, a heavy Fermi-liquid phase at $\xi > \xi_c$, a Kondo breakdown QCP ξ_c, and a fan-shaped region in the finite-temperature regime for finite N are in close resemblance to the phase diagram of the infinite-N case [see Fig. 1(a)] except for some quantitative changes such as the position of the QCP. Furthermore, we found that the first-order-like jump at the QCP still survives for the finite N, as indicated by the extrapolation of the solid circles in the finite-temperature phase diagram.

Magnetic susceptibility. Figures 16(a), 16(b), and 16(c) show the temperature-dependent local (momentum-integrated) spin susceptibility $\chi_{\rm loc}(T)/N$, the critical scaling of $\chi_{\rm loc}(T)/N$ in the quantum critical regime, and the uniform spin susceptibility $\chi_{\rm uni}(T)/N$. Regarding the uniform susceptibility when $\xi > \xi_c$, it exhibits a Curie-law behavior $\chi_{\rm uni}(T)/N \propto T^{-1}$ at high temperatures, where the local spin moments are unscreened, and then saturates at low temperatures when the local moments are completely screened. As ξ approaches the QCP, the $\chi_{\rm uni}$ is suppressed at intermediate temperatures. The qualitative features of the finite-N uniform susceptibility resemble the infinite-N results closely. The local susceptibility displays a crossover from a saturated Pauli susceptibility at low temperatures to a spin-liquid behavior in the intermediate-temperature range in the Kondo limit $\xi > \xi_c$. Above the spin-liquid region where $\Delta > 0$, the system shows a $1/T$ divergence in the local susceptibility at high temperatures. Within the finite-temperature quantum critical region, the scaled local spin susceptibility shows a power-law $(T/T^*)^{-0.023}$ quantum critical scaling in temperature, as shown in the dashed line in Fig. 16(b).

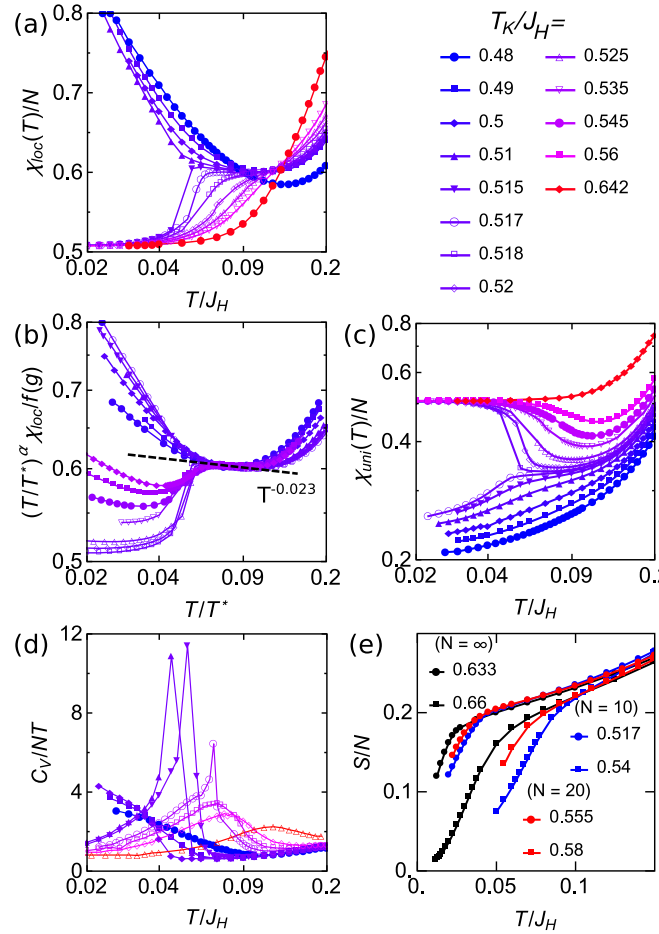

FIG. 16. (a) Temperature dependence of the local magnetic susceptibility $\chi_{\rm loc}(T)/N$ at different values of ξ. (b) Critical scaling of local susceptibility in the quantum critical regime is plotted in the logarithmic scale. T^* is the crossover temperature to the quantum critical region. (c) Uniform magnetic susceptibility $\chi_{\rm uni}(T)/N$ at different values of ξ. (d) Temperature dependence of C_V/NT at different values of ξ. (e) Shows the entropy per spin flavor, S/N, with different values ξ, for $N = \infty$ (black), $N = 10$ (red), and 20 (blue).

Entropy and specific-heat coefficient. The finite-N specific-heat coefficient and entropy per spin flavor are illustrated in Figs. 16(d) and 16(e), respectively. The qualitative behavior of the specific coefficient either at $\xi > \xi_c$ and $\xi < \xi_c$ shows a close resemblance to the infinite-N results: a plateau at low temperatures for $\xi > \xi_c$ associated with a linear-in-temperature entropy, i.e., $S/N \propto T$, a monotonic shrink of the range of the plateau as ξ approaches ξ_c from the Kondo side, and a "Schottky" peak above the FL region. Moreover, a weakly first-order jump at the QCP from the peak temperatures (solid circles in Fig. 6) is also observed in the finite-N results. The collapse of energy scales from both sides as the QCP is approached is clearly seen in the color map of the specific-heat coefficient (Fig. 6) with a fan-shaped quantum critical region. While including finite-N fluctuations, we found that the residual entropy in Fig. 16(e) still survives though is slightly decreased. We therefore suspect that this is more likely due to the local approximation rather than the neglect of $1/N$ corrections.

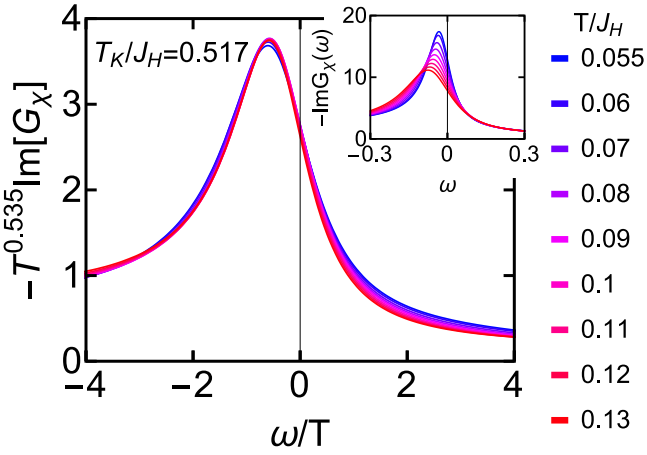

FIG. 17. The imaginary part of G_χ exhibits ω/T scaling behavior near the QCP ($T_K/J_H = 0.517$) for $N = 10$ and $K = 2$. Inset: ImG_χ without being scaled near the QCP.

ω/T scaling. The stability of the infinite-N results against the finite-N correction is further supported by the ω/T scaling of the critical fluctuation of the Kondo correlation in G_χ at the QCP for $N = 10$, i.e., $G''_\chi(\omega, T) = -T^{-0.535} f(\omega/T)$ with $f(\omega/T)$ being a universal function (see Fig. 17). Aside from the quantitative changes in $f(\omega/T)$ and the value of the critical exponent, the qualitative behavior of $f(\omega/T)$ for $N = 10$ is almost identical to the infinite-N case [see Fig. 3(e)]. Moreover, ω/T scaling of ImG_χ strongly suggests Kondo breakdown to occur at the QCP for the finite-N case.

In summary, we have performed self-consistent calculations of the Kondo-Heisenberg lattice model with finite values of N via including $1/N$ fluctuations. The global phase diagram, the ω/T scaling, and various physical observables we obtained here are in close resemblance to the infinite-N results except for some minor and quantitative changes. We thus conclude that the large-N approach we used here is a well-controlled method by $1/N$ corrections and the large-N results are able to correctly describe the qualitative features of the global phase diagram.

[1] L. Taillefer, Annu. Rev. Condens. Matter Phys. **1**, 51 (2010).

[2] See P. Coleman, *Heavy Fermions: Electrons at the Edge of Magnetism* (Wiley, New York, 2007); P. Gegenwart, Q. Si, and F. Steglich, Nat. Phys. **4**, 186 (2008).

[3] H. v. Löhneysen, A. Rosch, M. Vojta, and P. Wölfle, Rev. Mod. Phys. **79**, 1015 (2007).

[4] O. Trovarelli, C. Geibel, S. Mederle, C. Langhammer, F. M. Grosche, P. Gegenwart, M. Lang, G. Sparn, and F. Steglich, Phys. Rev. Lett. **85**, 626 (2000); J. Custers, P. Gegenwart, H. Wilhelm, K. Neumaier, Y. Tokiwa, O. Trovarelli, C. Geibel, F. Steglich, C. Pépin, and P. Coleman, Nature (London) **424**, 524 (2003); J. Custers, P. Gegenwart, C. Geibel, F. Steglich, P. Coleman, and S. Paschen, Phys. Rev. Lett. **104**, 186402 (2010).

[5] H. V. Löhneysen, T. Pietrus, G. Portisch, H. G. Schlager, A. Schröder, M. Sieck, and T. Trappmann, Phys. Rev. Lett. **72**, 3262 (1994).

[6] H. v. Löhneysen, S. Mock, A. Neubert, T. Pietrus, A. Rosch, A. Schröder, O. Stockert, U. Tutsch, J. Magn. Magn. Mater. **177**, 12 (1998).

[7] A. Schroder, G. Aeppli, R. Coldea, M. Adams, O. Stockert, H. Löhneysen, E. Bucher, R. Ramazashvili, and P. Coleman, Nature (London) **407**, 351 (2000).

[8] M. Klein, A. Nuber, F. Reinert, J. Kroha, O. Stockert, and H. v. Löhneysen, Phys. Rev. Lett. **101**, 266404 (2008); M. Klein, J. Kroha, H. v. Löhneysen, O. Stockert, and F. Reinert, Phys. Rev. B **79**, 075111 (2009).

[9] C. Petrovic, P. G. Pagliuso, M. F. Hundley, R. Movshovich, J. L. Sarrao, J. D. Thompson, Z. Fisk, and P. Monthoux, J. Phys.: Condens. Matter **13**, L337 (2001).

[10] Q. Y. Chen, D. F. Xu, X. H. Niu, J. Jiang, R. Peng, H. C. Xu, C. H. P. Wen, Z. F. Ding, K. Huang, L. Shu *et al.*, Phys. Rev. B **96**, 045107 (2017); S. Kirchner, S. Paschen, Q. Y. Chen, S. Wirth, D. L. Feng, J. D. Thompson, and Q. Si, Rev. Mod. Phys. **92**, 011002 (2020).

[11] O. Stockert, H. v. Löhneysen, A. Rosch, N. Pyka, and M. Loewenhaupt, Phys. Rev. Lett. **80**, 5627 (1998).

[12] O. Trovarelli, C. Geibel, C. Langhammer, S. Mederle, P. Gegenwart, F. M. Grosche, M. Lang, G. Sparn, F. Steglich, Physica B (Amsterdam) **281 & 282**, 372 (2000).

[13] Q. Si, S. Rabello, K. Ingersent, and J. L. Smith, Nature (London) **413**, 804 (2001).

[14] Q. Si and F. Steglich, Science **329**, 1161 (2010).

[15] S. Paschen, T. Lühmann, S. Wirth, P. Gegenwart, O. Trovarelli, C. Geibel, F. Steglich, P. Coleman, and Q. Si, Nature (London) **432**, 881 (2004); S. Friedemann, N. Oeschler, S. Wirth, C. Krellner, C. Geibel, F. Steglich, S. Paschen, S. Kirchner, and Q. Si, Proc. Natl. Acad. Sci. USA **107**, 14547 (2010).

[16] L. Prochaska, X. Li, D. C. MacFarland, A. M. Andrews, M. Bonta, E. F. Bianco, S. Yazdi, W. Schrenk, H. Detz, A. Limbeck *et al.*, Science **367**, 285 (2020).

[17] S. Seiro, L. Jiao, S. Kirchner, S. Hartmann, S. Friedemann, C. Krellner, C. Geibel, Q. Si, F. Steglich, and S. Wirth, Nat. Commun. **9**, 3324 (2018).

[18] J. Hertz, Phys. Rev. B **14**, 1165 (1976); A. J. Millis, **48**, 7183 (1993); A. Rosch, A. Schröder, O. Stockert, and H. v. Löhneysen, Phys. Rev. Lett. **79**, 159 (1997).

[19] E. Abrahams, and P. J. Wölfle, Proc. Natl. Acad. Sci. USA **109**, 3238 (2012).

[20] G. Lonzarich, D. Pines, and Y. F. Yang, Rep. Prog. Phys. **80**, 024501 (2017).

[21] M. T. Glossop and K. Ingersent, Phys. Rev. Lett. **99**, 227203 (2007); J.-X. Zhu, S. Kirchner, R. Bulla, and Q. Si, **99**, 227204 (2007).

[22] J.-X. Zhu, D. R. Grempel, and Q. Si, Phys. Rev. Lett. **91**, 156404 (2003); D. R. Grempel and Q. Si, **91**, 026401 (2003).

[23] M. T. Glossop, S. Kirchner, J. H. Pixley, and Q. Si, Phys. Rev. Lett. **107**, 076404 (2011).

[24] S. Burdin, D. R. Grempel, and A. Georges, Phys. Rev. B **66**, 045111 (2002); P. Sun and G. Kotliar, Phys. Rev. Lett. **91**, 037209 (2003); D. Tanasković, K. Haule, G. Kotliar, and V. Dobrosavljević, Phys. Rev. B **84**, 115105 (2011); P. Sun and G. Kotliar, Phys. Rev. Lett. **95**, 016402 (2005).

[25] C. Pépin, Phys. Rev. Lett. **94**, 066402 (2005); T. Senthil, S. Sachdev, and M. Vojta, **90**, 216403 (2003).
[26] L. Zhu, S. Kirchner, Q. Si, and A. Georges, Phys. Rev. Lett. **93**, 267201 (2004).
[27] Y. Y. Chang, S. Paschen, and C. H. Chung, Phys. Rev. B **97**, 035156 (2018); Y. Y. Chang, F. Hsu, S. Kirchner, C. Y. Mou, T. K. Lee, and C. H. Chung, **99**, 094513 (2019).
[28] J. Rech, P. Coleman, G. Zarand, and O. Parcollet, Phys. Rev. Lett. **96**, 016601 (2006).
[29] Y. Komijani and P. Coleman, Phys. Rev. Lett. **120**, 157206 (2018).
[30] Y. Komijani and P. Coleman, Phys. Rev. Lett. **122**, 217001 (2019).
[31] N. Read and D. M. Newns, J. Phys. C: Solid State Phys. **16**, 3273 (1983).
[32] D. P. Arovas and A. Auerbach, Phys. Rev. B **38**, 316 (1988); O. Parcollet and A. Georges, Phys. Rev. Lett. **79**, 4665 (1997).
[33] E. Lebanon, P. Coleman, Phys. Rev. B **76**, 085117 (2007); E. Lebanon, J. Rech, P. Coleman, O. Parcollet, Phys. Rev. Lett **97**, 106604 (2006).
[34] S. Sachdev, Phys. Rev. B **45**, 12377 (1992).
[35] For $\kappa > \kappa_c = 0.4$, the pure AF Heisenberg interaction in the large-N limit favors AF LRO. See S. Sachdev, *Quantum Phase Transitions of Antiferromagnets and the Cuprate Superconductors* (Springer, Heidelberg, 2012).
[36] A. Auerbach, *Interacting Electrons and Quantum Magnetism* (Springer, Heidelberg, 1994).
[37] A. Gelfert and W. Nolting, J. Phys.: Condens. Matter **13**, R505 (2001).
[38] P. Coleman, I. Paul, and J. Rech, Phys. Rev. B **72**, 094430 (2005).
[39] T. N. De Silva, M. Ma, and F. C. Zhang, Phys. Rev. B **66**, 104417 (2002).
[40] Weakly first-order transitions exist in the Schwinger boson mean-field theories due to the attractive quartic term $O(\Delta^4)$. This term can be canceled by including a small repulsive biquadratic term $J'_H(\boldsymbol{S}_i \cdot \boldsymbol{S}_j)^2$ with $J'_H \ll J_H$ and thus the second-order phase transitions can be restored [29].
[41] A. Auerbach and D. P. Arovas, Phys. Rev. Lett. **61**, 617 (1988); S. Winterfeldt and D. Ihle, Phys. Rev. B **56**, 5535 (1997).
[42] A. C. Hewson, *The Kondo Problem to Heavy Fermions* (Cambridge University Press, Cambridge, England, 1997), Vol. 2.
[43] J. H. Pixley, S. Kirchner, K. Ingersent, and Q. Si, Phys. Rev. Lett. **109**, 086403 (2012).
[44] Nonetheless, this LRO will be stablized as 3D LRO in real materials due to weak interlayer coupling and the calculated 2D LRO will become quasi-long-range order in the corresponding renormalized classical regime, see S. Chakravarty, B. I. Halperin, and D. R. Nelson, Phys. Rev. B **39**, 2344 (1989).
[45] J. F. Wang and Y. F. Yang, arXiv:2009.00543.
[46] A. Ramires and P. Coleman, Phys. Rev. B **93**, 035120 (2016).
[47] N. Andrei and C. Destri, Phys. Rev. Lett. **52**, 364 (1984); A. M. Tsvelik and P. B. Wiegmann, Z. Phys. B **54**, 201 (1984); A. W. Ludwig and I. Affleck, Nucl. Phys. B **428**, 545 (1994).
[48] S. Sachdev and J. Ye, Phys. Rev. Lett. **69**, 2411 (1992); A. Georges, O. Parcollet, and S. Sachdev, Phys. Rev. B **63**, 134406 (2001); J. Maldacena and D. Stanford, Phys. Rev. D **94**, 106002 (2016).
[49] P. Goswami and Q. Si, Phys. Rev. B **89**, 045124 (2014).
[50] Nevertheless, for the realistic quasi-2D ($D > 2$) layered materials we focus on here, the BKT physics is expected not to play a significant role.
[51] B. H. Bernhard and C. Lacroix, Phys. Rev. B **92**, 094401 (2015).
[52] T. T. Ong and B. A. Jones, Phys. Rev. Lett. **103**, 066405 (2009).